nature chemistry

ARTICLES

https://doi.org/10.1038/s41557-018-0015-x

O_2–O_2 and O_2–N_2 collision-induced absorption mechanisms unravelled

Tijs Karman[1], Mark A. J. Koenis[2], Agniva Banerjee[1], David H. Parker[1], Iouli E. Gordon[3], Ad van der Avoird[1], Wim J. van der Zande[1] and Gerrit C. Groenenboom[1]*

Collision-induced absorption is the phenomenon in which interactions between colliding molecules lead to absorption of light, even for transitions that are forbidden for the isolated molecules. Collision-induced absorption contributes to the atmospheric heat balance and is important for the electronic excitations of O_2 that are used for remote sensing. Here, we present a theoretical study of five vibronic transitions in O_2–O_2 and O_2–N_2, using analytical models and numerical quantum scattering calculations. We unambiguously identify the underlying absorption mechanism, which is shown to depend explicitly on the collision partner—contrary to textbook knowledge. This explains experimentally observed qualitative differences between O_2–O_2 and O_2–N_2 collisions in the overall intensity, line shape and vibrational dependence of the absorption spectrum. It is shown that these results can be used to discriminate between conflicting experimental data and even to identify unphysical results, thus impacting future experimental studies and atmospheric applications.

The selection rules that govern atomic and molecular spectroscopy are related to symmetry restrictions, which imply vanishing transition strength to a certain degree of approximation. Symmetry is broken by collisions with other molecules in the gas phase, which lifts the selection rules and induces otherwise forbidden electric dipole transitions, leading to so-called collision-induced absorption[1]. Collision-induced absorption was discovered by Welsh and co-workers for forbidden vibrational transitions in compressed O_2 and N_2 gases[2]. More recent measurements of collision-induced absorption typically use cavity ring-down spectroscopy to observe the weak collision-induced signal by achieving long path lengths[3–11], rather than high pressures[12,13]. Roto-translational collision-induced absorption is important for the atmospheric heat balance[14], and electronic transitions in O_2, such as the A-band $X^3\Sigma_g^- \rightarrow b^1\Sigma_g^+(v'=0)$ transition[15–19] and the 1.27 μm band $X^3\Sigma_g^- \rightarrow a^1\Delta_g(v'=0)$ transition[20], have gained significant attention as they are observable in Earth's atmosphere and used in remote sensing calibration. Absorption for these transitions is due to spin–orbit-allowed magnetic dipole lines, but collision-induced absorption also contributes significantly. Oxygen collision-induced absorption has also been put forward as a biomarker to be observed in exo-planetary atmospheres[21], where the quadratic pressure dependence can be used to probe the atmospheric distribution, in addition to the column density.

The theoretical treatment of collision-induced absorption is well established for rotation–translation and vibrational transitions[1], and it is well known that such spectra are typically dominated by quadrupole induced dipole moments. Electronic transitions have been studied theoretically for forbidden $^1S \rightarrow {}^1D$ transitions in atom–atom collisions[22,23], and the mechanism is again quadrupole induction. By contrast, for spin-forbidden electronic transitions, the mechanism cannot be only quadrupole induction, as this interaction does not lift the spin selection rule. Mechanisms for breaking spin symmetry have been suggested[24–30], but not identified in absorption spectra, despite extensive experimental studies. The most extensively studied spin-forbidden transitions are electronic transitions of molecular oxygen. In 1885, Janssen first observed the oxygen A-band in dense gases[31,32], long before the process was identified as collision-induced absorption[33]. More recently, atmospheric applications have motivated numerous experimental studies, which observe both monomer absorption lines and collision-induced absorption[3–13,34–36]. A line shape theory does not yet exist, neither for spin-forbidden transitions nor for collision-induced molecular electronic transitions in general.

Here, we theoretically study the $X^3\Sigma_g^- \rightarrow a^1\Delta_g$ and $X^3\Sigma_g^- \rightarrow b^1\Sigma_g^+$ transitions of molecular oxygen in O_2–O_2 and O_2–N_2 collisions. These transitions are monomer-forbidden by both spin ($S=1 \nrightarrow 0$) and spatial ($g \nrightarrow g$) selection rules. The most influential monograph on collision-induced absorption states the following about these specific transitions[1]: 'For collisional induction of these bands a foreign molecule is more or less as expedient as an O_2 molecule. The specific properties of the collisional partner hardly matter as long as it is not absent.' In this Article, however, we show that the underlying absorption mechanism depends on the specific properties of the collisional partner and that this leads to qualitative differences in the intensity, line shape and vibrational dependence of the absorption spectra. To this end, we present the first theoretical line shape study of electronic transitions in molecular collision-induced absorption.

In a bimolecular collision, the symmetry of the system is broken and the spatial selection rules are relaxed. However, this does not lift the selection rule on spin multiplicity. Three different mechanisms have been proposed to break the spin symmetry:

The first mechanism, the spin–orbit mechanism, takes into account the intramolecular spin–orbit coupling between the $X^3\Sigma_g^-, \Omega=0^+$ and $b^1\Sigma_g^+$ states of O_2, which mixes these states with coefficient $C=0.0134i$. This mixing of singlet and triplet electronic states lifts the spin selection rules[25–28]. This leads to spin–orbit-allowed magnetic dipole and electric quadrupole transition moments and the associated monomer absorption lines. In a collision complex, the breaking of spin symmetry leads to transition dipole moments, through quadrupole induction. This dipole moment is long ranged and varies with R^{-4}, where R is the intermolecular distance.

[1]Institute for Molecules and Materials, Radboud University, Nijmegen, the Netherlands. [2]Van 't Hoff Institute for Molecular Sciences, University of Amsterdam, Amsterdam, the Netherlands. [3]Harvard-Smithsonian Center for Astrophysics, Cambridge, MA, USA. *e-mail: gerritg@theochem.ru.nl

The second mechanism, the exchange mechanism, applies only to paramagnetic collision partners. In this case, the total electron spin of the collision complex is conserved, making the transition formally allowed, even though the O_2 monomer spin changes from triplet to singlet. For example, for the O_2–O_2 collisions considered here,

$$O_2(X^3\Sigma_g^-) + O_2(X^3\Sigma_g^-) + h\nu \rightarrow O_2(a^1\Delta_g / b^1\Sigma_g^+) + O_2(X^3\Sigma_g^-).$$

The final state is a total spin triplet state of the complex, whereas the initial state has two triplet molecules, which can couple to overall singlet, triplet and quintet spin states. For transitions between triplet states, the formal spin restriction has been lifted. Non-zero intensity for this process is due to the exchange interaction between paramagnetic collision partners[24], and the induced dipole moment decays exponentially with the intermolecular distance, as $\exp(-\gamma R)$.

The heavy-atom effect is a possible third mechanism, where interaction with a heavier element enhances relativistic effects such as spin–orbit coupling[25,29,30]. This mechanism is not considered here because it is less relevant for collisions with light atmospherically abundant collision partners such as N_2 and O_2.

Results

Theory. We calculated bimolecular collision-induced absorption spectra for the $X^3\Sigma_g^- \rightarrow a^1\Delta_g$ and $b^1\Sigma_g^+$ transitions in O_2–O_2 and O_2–N_2, for both the exchange and spin–orbit mechanisms. Such line shape calculations, which have previously been performed only for roto-translational and vibrational (RT&V) transitions, obtain the absorption spectrum from dipole coupling between the scattering wavefunctions that describe the colliding molecules, which are calculated using coupled-channels theory[1]. These calculations require the electronic energy and transition dipole moments for the electronic ground and six electronically excited states of the complex as a function of the nuclear coordinates. We calculated these four-dimensional potential energy and exchange-induced transition dipole moment surfaces using ab initio electronic structure methods[37]. The essential innovation that enabled these calculations was diabatization of these surfaces, which includes non-adiabatic couplings beyond the Born–Oppenheimer approximation. To this end, we used a novel multiple-property-based diabatization algorithm, which has been developed as a part of this project[38]. This treatment is crucial due to the occurrence of seams of conical intersections at which derivative couplings are divergent. The issue of diabatization is not encountered for RT&V dipole surfaces, which involve only the electronic ground state. Similarly unfamiliar from RT&V transitions is the first-principles computation of intermolecular exchange-induced properties, which is virtually unexplored[39], and is shown here to be challenging. For the spin–orbit mechanism, we employ the long-range model that we developed in ref. [40], which involves the spin–orbit-induced transition quadrupole moment of O_2. In this work, scattering wavefunctions are calculated in the approximation of an isotropic interaction between the colliding molecules. This allows decoupling of the radial and angular degrees of freedom and the latter to be treated analytically, thus significantly reducing the computational effort. The isotropic approximation applies only to the interaction potential, whereas the full anisotropic transition dipole surface is used. This approximation is commonly used in line shape calculations for RT&V bands, and we have extended this theory to electronic transitions[40]. We also present corrections to this approximation from classical statistical mechanics, using the full anisotropic interaction. Numerical results suggest that the effect of anisotropy is more pronounced for electronic transitions than for RT&V bands. A more detailed discussion of all the calculations is provided in the Supplementary Information and supporting references[37,38,40].

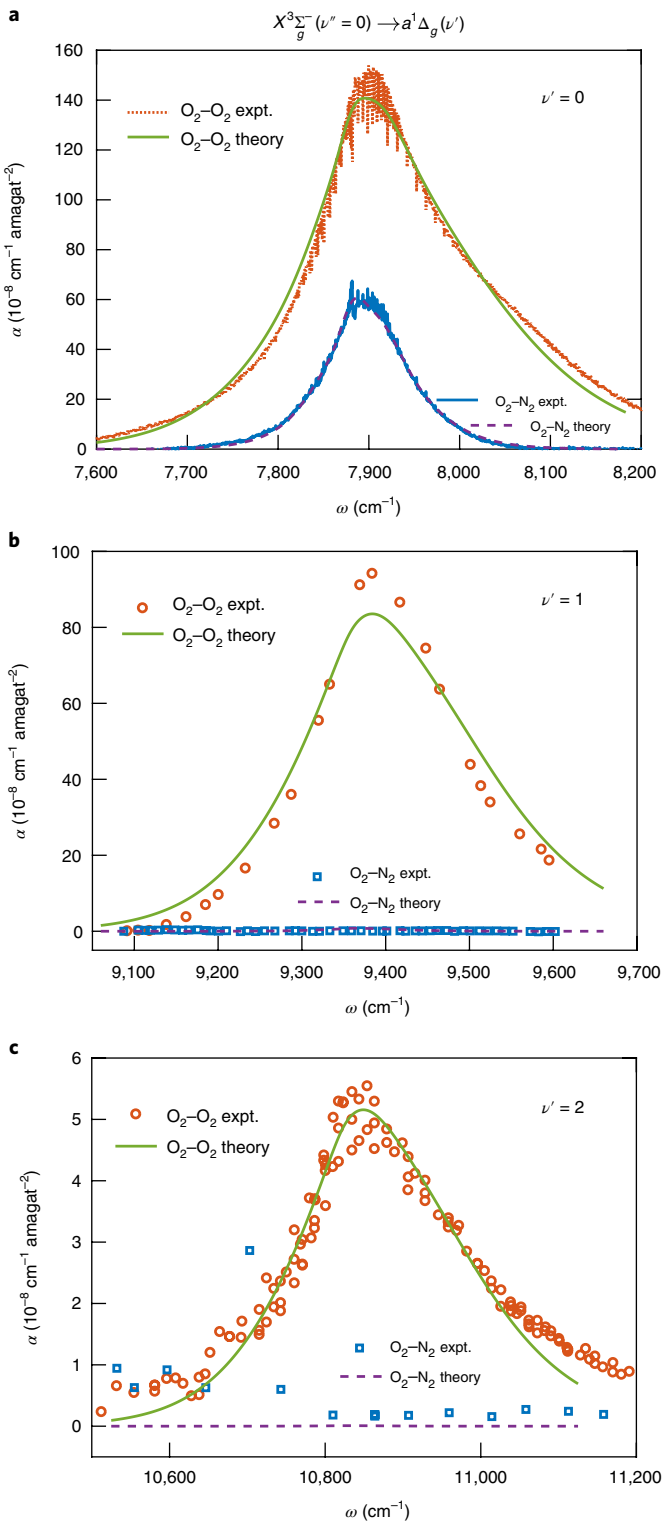

Fig. 1 | Experimental and theoretical collision-induced absorption spectra for the $X^3\Sigma_g^-(v''=0) \rightarrow a^1\Delta_g(v')$ bands of O_2–O_2 and O_2–N_2. a–c, Spectra corresponding to $v'=0$ (**a**), 1 (**b**) and 2 (**c**), where experimental data are taken from ref. [4], this work and ref. [9], respectively. The absorption coefficient, α, is normalized to the square of the number density, which is measured in amagat, the number density of an ideal gas at 1 atm and 0 °C. Absorption by O_2–O_2 is more intense and broader in frequency than for O_2–N_2. Vibrational transitions $v'>0$ are observed for O_2–O_2 but not for O_2–N_2. The intensity for the spin–orbit mechanism follows the predicted scaling with Franck–Condon factors, whereas the suppression is evidently less strong for the exchange contribution, which only contributes for O_2–O_2.

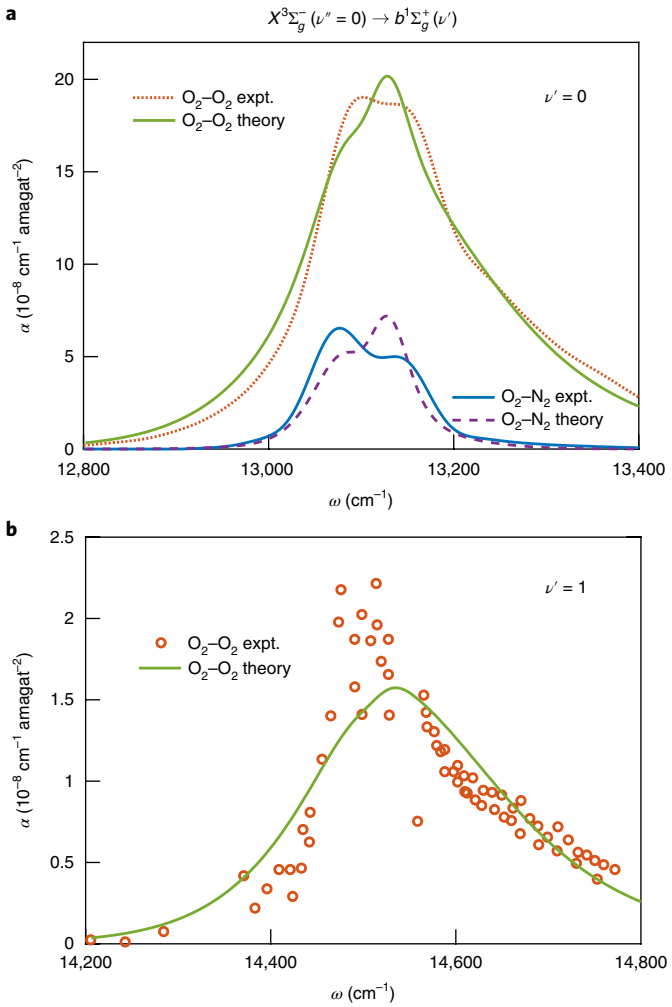

Fig. 2 | Experimental and theoretical collision-induced absorption spectra for the $X^3\Sigma_g^-(v''=0) \rightarrow b^1\Sigma_g^+(v')$ bands of O_2–O_2 and O_2–N_2. a,b, Spectra corresponding to $v'=0$ (**a**) and 1 (**b**), where experimental data are taken from ref. [7] and ref. [12], respectively. Absorption by O_2–O_2 is more intense and broader in frequency than for O_2–N_2.

Figures 1 and 2 present collision-induced absorption spectra for $X^3\Sigma_g^- \rightarrow a^1\Delta_g$ and $X^3\Sigma_g^- \rightarrow b^1\Sigma_g^+$ transitions, respectively. The $a^1\Delta_g(v'=1)$ band was measured in this work using cavity ring-down spectroscopy, similar to the method used in ref. [6], and is described in more detail in Supplementary Section 6. Experimental data for the $a^1\Delta_g(v'=0, 2)$ and $b^1\Sigma_g^+(v'=0, 1)$ bands are taken from refs [4,7,9,12], and are the HITRAN recommended data wherever multiple experiments exist[41,42]. The theoretical line shapes match the experimental results well. However, to also achieve agreement for the intensities, the theory was scaled by the factors shown in Table 1. The scaling factors for the exchange mechanism, c_{Exch}, seem large, but, as shown below, they are within the uncertainty of the calculated intensity (which is due to the large uncertainty of the dipole surfaces for this mechanism). The predicted line shapes are unaffected by this uncertainty. For the spin–orbit mechanism, where the dipole surface is known more accurately, the anisotropy-corrected scaling factors are closer to unity.

Intensity. From the absorption spectra in Figs. 1 and 2, qualitative differences between O_2–O_2 and O_2–N_2 collision-induced absorption become apparent. The O_2–O_2 contributions are typically more intense, significantly broader in frequency, and decay less rapidly

Table 1 | Scale factors for theoretical line shapes fit to experimental data

Transition	$c_{Exch}^{O_2-O_2}$	$c_{SO}^{O_2-O_2}$	$c_{SO}^{O_2-N_2}$
$X^3\Sigma_g^- \rightarrow a^1\Delta_g(v'=0)$	4.48	1.10	1.68
$X^3\Sigma_g^- \rightarrow a^1\Delta_g(v'=1)$	2.90		
$X^3\Sigma_g^- \rightarrow a^1\Delta_g(v'=2)$	0.15		
$X^3\Sigma_g^- \rightarrow b^1\Sigma_g^+(v'=0)$	6.41	0.66	0.71
$X^3\Sigma_g^- \rightarrow b^1\Sigma_g^+(v'=1)$	0.63		

Scaling factors are shown for both the exchange (Exch) and spin-orbit (SO) mechanisms. Classical statistical mechanical corrections for anisotropic interactions have been included (Supplementary Section 3).

with increasing vibrational excitation v'. The difference in line shape is seen even more clearly on a logarithmic scale (Fig. 5). The observed difference in intensity can be understood as the O_2–N_2 intensity is solely due to the spin–orbit mechanism, whereas the O_2–O_2 intensity is dominated by the additional exchange mechanism, and the contribution of the spin–orbit mechanism is observable only near the line centre.

Line shape. The difference in line shape can also be understood from these mechanisms and the correspondingly different geometry dependence of the transition dipole moment. The dipole moment of the spin–orbit mechanism, which is the only contribution for O_2–N_2, results from long-range spin–orbit-induced quadrupole induction and depends on the intermolecular distance, R, as R^{-4}. This drives electronic transitions at comparatively long length scales—and therefore long timescales—which leads to a relatively narrow absorption feature. By contrast, the dipole moment of the exchange mechanism, which dominates for O_2–O_2, decays exponentially with intermolecular distance. This induces electronic transitions at very short length and timescales, leading to a much broader absorption spectrum.

To rigorously demonstrate the relation between line shape and absorption mechanism, we considered an analytical model for the translational profile, VG, which determines the absorption line shape (Supplementary Section 1e). This model accounts for hard-sphere scattering (with radius a) at a single energy $E=k_BT$ and dipole functions proportional to $\exp(-\gamma R)$ and R^{-4}, respectively. This yields for the exchange (Exch) and spin-orbit (SO) mechanisms:

$$VG_{Exch}(\omega) = \frac{\gamma^2 k k'}{\{(\gamma^2+k^2)^2 + 2(\gamma^2-k^2)k'^2 + k'^4\}^2}$$
$$VG_{SO}(\omega) = \frac{1}{kk'}\left[G_{1,3}^{3,1}\left(\frac{a^2}{4}[k-k']^2 \;\middle|\; \begin{matrix} 0 \\ 0 \end{matrix} \; \begin{matrix} \frac{3}{2} \\ \end{matrix} \; \begin{matrix} 2 \\ \end{matrix}\right)\right]^2 \quad (2)$$

where $G_{1,3}^{3,1}$ denotes a Meijer G function[43] and the initial- and final-state wavenumbers are given by $k=\sqrt{2\mu k_BT}$ and $k'=\sqrt{2\mu(k_BT+\hbar\omega)}$, respectively. These profiles are compared to the results of the full calculations in Fig. 3, using realistic parameters $a=7a_0$ and $\gamma=3a_0^{-1}$. The analytical model reproduces the typical translational profiles, supporting the length-scale argument presented above.

Vibrational dependence. The differences in v' dependence, seen in Figs. 1 and 2, are explained by the vibrational dependence of the transition dipole moments. In the spin–orbit mechanism, the only contribution for O_2–N_2, the dipole moment is proportional to the spin–orbit-induced transition quadrupole moment of O_2.

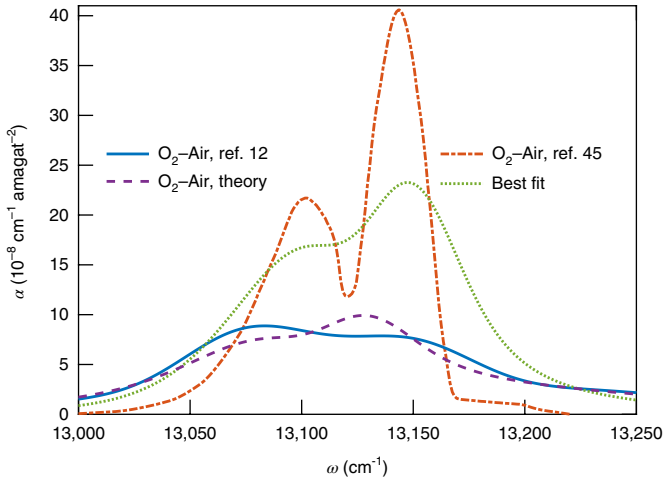

Fig. 3 | Collision-induced absorption spectra for the $X^3\Sigma_g^-(v''=0) \rightarrow b^1\Sigma_g^+(v'=0)$ band in air, normalized to the product of O_2 and air number densities. The experimental spectra of ref. [12] and of the more recent ref. [45] differ significantly. The line shape of ref. [45] is even narrower than the theoretical line shape for the spin–orbit mechanism, which is indicated as the best fit. A narrower line shape requires a dipole moment of longer range than R^{-4}, which is unphysical.

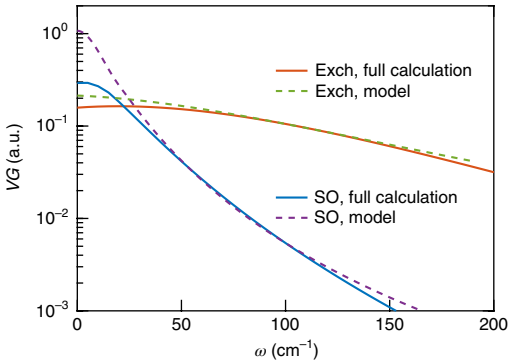

Fig. 4 | Translational profiles for the $X^3\Sigma_g^- \rightarrow a^1\Delta_g$ transition for both exchange and spin–orbit mechanisms. Results of the full line shape calculation are compared to the results of the analytical hard-sphere model (discussed in detail in Supplementary Section 1e) for both the exchange (Exch) and spin-orbit (SO) mechanisms. The analytical model describes the decay in the wing well, indicating that the line shape is determined by the range of the induced dipole moment.

This transition quadrupole moment is only weakly dependent on the O_2 bond length, and so the intensities of transitions to $v'>0$ are suppressed following the Franck–Condon factors. For the bands studied here, the Franck–Condon factors are small, ranging from 1×10^{-4} to 7×10^{-2} (ref. [44]). Therefore, the $v'>0$ transitions are heavily suppressed for O_2–N_2 and are not observed. For the exchange mechanism, which is dominant for O_2–O_2, the vibrational dependence is evidently much stronger, as $v'>0$ bands are suppressed by much less than the Franck–Condon factor. This can be understood as the transition dipole moment for this mechanism depends on the nuclear geometry—including vibrational coordinates—with exponential sensitivity. This is shown by exploratory electronic structure calculations, presented in Supplementary Section 2, which yield a vibrational dependence that is in qualitative agreement with the scaling factors in Table 1.

Analysis of experimental spectra. The insight into the absorption mechanism and resulting spectral signatures developed in the previous sections can be used to analyse conflicting experimental line shapes. This is illustrated in Fig. 4, which shows collision-induced absorption spectra for the oxygen A-band $X^3\Sigma_g^- \rightarrow b^1\Sigma_g^+(v'=0)$ transition in air, that is, 21% O_2 and 79% N_2. The experimental results in ref. [12] and the theoretical spectrum correspond to those shown in Fig. 2a. Figure 4 also contains data from the recent multispectrum fitting study of ref. [45]. The experimental spectra differ significantly, and the line shape of ref. [45] is narrower and more structured. The collision-induced line shape of ref. [45] is even narrower than the narrowest theoretical result, corresponding to the R^{-4} spin–orbit mechanism, indicated as 'Best fit' in Fig. 4. This implies that the line shape of ref. [45] can only be reproduced by assuming a transition dipole moment that has an even longer range than R^{-4}; that is, the line shape is unphysically narrow.

By contrast, the widths of the spectra of ref. [12] match the theoretical predictions well, for both O_2–O_2 and O_2–N_2. However, deviations between theory and the experiment of ref. [12] are observed in the structure near the band centre, which is also visible in Fig. 2a. In the theoretical spectra, the high-frequency wing is always more intense than the low-frequency wing due to the detailed balance relation developed in Supplementary Section 1g, which the experimental spectrum is seen to violate. This approximate detailed balance relation assumes a weak dependence of the potential on the electronic state.

In the experiments compared above, the total absorption is measured directly, and the experimental collision-induced absorption spectra are obtained by subtracting a line-by-line model of the monomer absorption. This analysis can lead to a dependence of the extracted collision-induced absorption on line-by-line parameters such as line mixing[12,45]. Analysis of experimental spectra is particularly difficult for the A-band, where the differences between experiment and theory are largest, because collision-induced absorption is weakest and magnetic dipole lines are strongest for this transition. Thus, the marked deviations from theory do not disqualify either measurement; rather they expose the limitations of the line-by-line absorption models employed and issues with parameter correlation. In this context, the presented line shape theory is a useful constraint on experimental data, which could improve fitting and extrapolation of measured absorption and hence further improve the accuracy of atmospheric measurements.

Discussion

Finally, we estimated the uncertainty of our calculations, which had two sources. First, the scattering dynamics is treated approximately, using isotropic interaction potentials. Second, the used potential energy and transition dipole moment surfaces are inexact.

Including interaction anisotropy in quantum-mechanical line shape calculations is prohibitively computer intensive[46] and not attempted here. Yet, we can provide estimates of the effects of interaction anisotropy from a classical statistical mechanical theory, as used in ref. [47] and discussed in more detail in Supplementary Section 3. We note that quantum corrections to this formalism are available[48], but have not been included. In this theory, the integrated intensity—but not the line shape—is calculated from a thermal average of the squared transition dipole moment. These integrals over the dimer configuration space can be performed using either isotropic or anisotropic potentials, and the ratio of these results provides an estimate of the effect of anisotropy on the intensity. We find that anisotropic interactions enhance the intensity by a factor of 2 to 4 for the bands considered here, indicating that full inclusion of anisotropy is necessary to reproduce the experiment. We note that, when this procedure is applied to the roto-translational band of N_2–N_2, we find 20% enhancement of the intensity at $T=78$ K, but essentially no effect at room temperature, in agreement with the

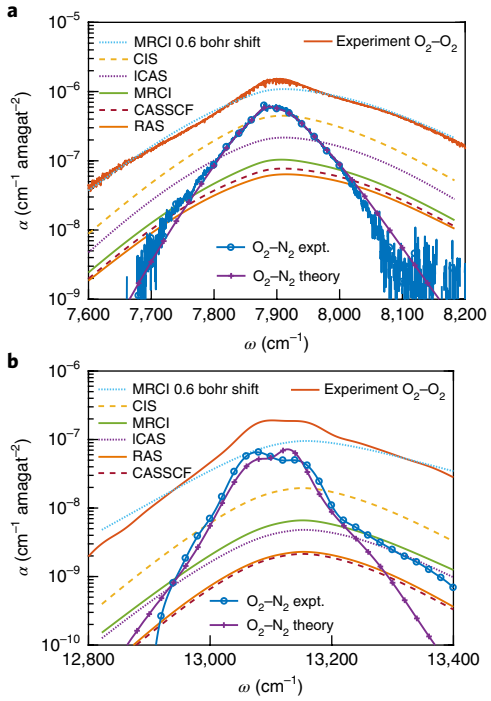

Fig. 5 | Collision-induced absorption spectra for the $X^3\Sigma_g^- \rightarrow a^1\Delta_g$ and $b^1\Sigma_g^+$ transitions in O_2–O_2 and experimental results. a,**b**, Experimental spectra in panels **a** and **b** are from ref. [4] and ref. [12], respectively. Theoretical spectra based on the exchange mechanism are calculated using various dipole moment surfaces, as indicated in the legend in the figure. These predictions differ by an order of magnitude in intensity but predict identical line shapes, which differ substantially from the more narrow O_2–N_2 results included for comparison.

full line shape calculations of ref. [46]. To further investigate the effect of anisotropy, we performed line shape calculations using a radially shifted isotropic potential. As shown in Fig. 5, agreement of the total intensity requires a shift of 0.6–0.7a_0, which is small compared to the neglected anisotropy of the classical turning point of the potential, which varies between 7.5a_0 for collinear geometries and 5.4a_0 for parallel orientations. These results suggest that the effect of anisotropy may be more substantial for the electronic transitions studied here than for their well-studied roto-translational counterparts.

The accuracy of our calculations was further affected by the accuracy of the transition dipole surfaces. To give an estimate of the associated uncertainty, we calculated the absorption spectra with **a** number of dipole surfaces, as shown in Fig. 5. This includes the MRCI and CASSCF dipole surfaces of ref. [37] and additional surfaces denoted CIS, *l*CAS and RAS, calculated in the present work. A more detailed description is provided in Supplementary Section 4. The methods used to calculate these transition dipole moment surfaces differ only in the treatment of electron correlation, and the observed differences represent a rather surprising result. Dipole moments for allowed transitions are typically accurately calculated at low levels of theory, as they are of one-electron character and hence insensitive to hard-to-treat effects such as electron correlation. The transitions studied here are induced by the intermolecular exchange interaction and are not simple one-electron transitions, so the effects of electron correlation are surprisingly pronounced. The predicted intensities differ by factors up to 10, so the scaling factors of Table 1 are within the 'theoretical error bars'. More importantly, the predicted line shape is unaffected by this uncertainty, which motivates the analysis in terms of theoretical line shapes but not intensities, presented in this Article. This can be understood from analysis of the line shape, presented in Supplementary Section 1c. The line shape is sensitive to the exp($-\gamma R$) decay with intermolecular separation R, but is affected less by the intensity and anisotropy of the dipole surface, which remain uncertain.

Conclusions

In conclusion, we have presented the first line shape calculations for spin-forbidden electronic transitions in bimolecular collisions, which permit the unambiguous identification of the absorption mechanism for the $X^3\Sigma_g^- \rightarrow a^1\Delta_g(v'=0,1,2)$ and $b^1\Sigma_g^+(v'=0,1)$ bands in O_2–O_2 and O_2–N_2. The absorption mechanism is shown to depend on the specific properties of the collision partner, which contradicts the conventional wisdom in the field[1]. Only if the perturbing molecule has non-zero electron spin does an intermolecular-exchange mechanism contributes to the absorption, in addition to a spin–orbit-based mechanism. As a result, the O_2–O_2 absorption spectra—when compared to O_2–N_2—are more intense, broader in frequency and decay less rapidly with v', violating the v' dependence expected from Franck–Condon factors. These spectral signatures of the absorption mechanism are reproduced by our ab initio calculations and are explained by the difference in range—R^{-4} versus exp($-\gamma R$)—of the induced transition dipole moment for the two underlying absorption mechanisms. The radial dependence of these mechanisms is not specific to the studied systems, so our conclusions are more generally applicable. The presented results impact experimental studies, where analysis of the spectral line shape allows the relative contribution of the underlying absorption mechanisms to be extracted and even to identify unphysical results, as illustrated for conflicting experimental data for the oxygen A-band[12, 45]. Furthermore, this study motivates the development of electronic structure methods to calculate converged exchange-induced transition dipole moments, which presently have surprisingly large theoretical error bars due to the sensitivity to electron correlation.

Data availability. All measured and calculated absorption spectra are available in the Supplementary Information.

Received: 18 September 2017; Accepted: 23 January 2018;
Published online: 09 April 2018

References

1. Frommhold, L. *Collision-Induced Absorption in Gases* (Cambridge Univ. Press, Cambridge, 1994).
2. Crawford, M. F., Welsh, H. L. & Locke, J. L. Infra-red absorption of oxygen and nitrogen induced by intermolecular forces. *Phys. Rev.* **75**, 1607–1607 (1949).
3. Smith, K. M. & Newnham, D. A. Near-infrared absorption cross sections and integrated absorption intensities of molecular oxygen (O_2, O_2–O_2, and O_2–N_2). *J. Geophys. Res. Atmos.* **105**, 7383–7396 (2000).
4. Maté, B., Lugez, C., Fraser, G. T. & Lafferty, W. J. Absolute intensities for the O_2 1.27 μm continuum absorption. *J. Geophys. Res. Atmos.* **104**, 30585–30590 (1999).
5. Long, D. A., Robichaud, D. J. & Hodges, J. T. Frequency-stabilized cavity ring-down spectroscopy measurements of line mixing and collision-induced absorption in the O_2 A-band. *J. Chem. Phys.* **137**, 014307 (2012).
6. Spiering, F. R. et al. Line mixing and collision induced absorption in the oxygen A-band using cavity ring-down spectroscopy. *J. Chem. Phys.* **133**, 114305 (2010).
7. Spiering, F. R., Kiseleva, M. B., Filippov, N. N., van Kesteren, L. & van der Zande, W. J. Collision-induced absorption in the O_2 B-band region near 670 nm. *Phys. Chem. Chem. Phys.* **13**, 9616–9621 (2011).
8. Spiering, F. R. et al. The effect of collisions with nitrogen on absorption by oxygen in the A-band using cavity ring-down spectroscopy. *Mol. Phys.* **109**, 535–542 (2011).
9. Spiering, F. R. & van der Zande, W. J. Collision induced absorption in the $a^1\Delta(v=2) \leftarrow X^3\Sigma_g^-(v=0)$ band of molecular oxygen. *Phys. Chem. Chem. Phys.* **14**, 9923–9928 (2012).
10. Sneep, M. & Ubachs, W. Cavity ring-down measurement of the O_2–O_2 collision-induced absorption resonance at 477 nm at sub-atmospheric pressures. *J. Quant. Spectrosc. Radiat. Transf.* **78**, 171–178 (2003).

11. Sneep, M. & Ubachs, W. in *Weakly Interacting Molecular Pairs: Unconventional Absorbers of Radiation in the Atmosphere* Vol. 27 (eds Camy-Peret, C. & Vigasin, A.) 203–211 (NATO Science Series: IV: Earth and Environmental Sciences, Springer, 2003).
12. Tran, H., Boulet, C. & Hartmann, J.-M. Line mixing and collision-induced absorption by oxygen in the A-band: laboratory measurements, model, and tools for atmospheric spectra computations. *J. Geophys. Res.* **111**, D15210 (2006).
13. Vangvichith, M., Tran, H. & Hartmann, J.-M. Line-mixing and collision induced absorption for O_2CO_2 mixtures in the oxygen A-band region. *J. Quant. Spectrosc. Radiat. Transf.* **110**, 2212–2216 (2009).
14. Höpfner, M., Milz, M., Buehler, S., Orphal, J. & Stiller, G. The natural greenhouse effect of atmospheric oxygen (O_2) and nitrogen (N_2). *Geophys. Res. Lett.* **39**, L10706 (2012).
15. Eldering, A. et al. High precision atmospheric CO_2 measurements from space: the design and implementation of OCO-2. In *Proc. 2012 IEEE Aerospace Conference* 1–10 (IEEE, 2012).
16. Miller, C. E. et al. Precision requirements for space-based data. *J. Geophys. Res. Atmos.* **112**, D10314 (2007).
17. Kuang, Z., Margolis, J. S., Toon, G. C., Crisp, D. & Yung, Y. L. Spaceborne measurements of atmospheric CO_2 by high-resolution nir spectrometry of reflected sunlight: an introductory study. *Geophys. Res. Lett.* **29**, 1716 (2002).
18. O'Brien, D. M., Mitchell, R. M., English, S. A. & Costa, G. A. D. Airborne measurements of air mass from O_2 A-band absorption spectra. *J. Atmos. Ocean. Technol.* **15**, 1272–1286 (1998).
19. Diedenhoven, Bv, Hasekamp, O. P. & Aben, I. Surface pressure retrieval from SCIAMACHY measurements in the O_2 A-band: validation of the measurements and sensitivity on aerosols. *Atmos. Chem. Phys.* **5**, 2109–2120 (2005).
20. Wunch, D. et al. The total carbon column observing network. *Philos. Trans. R. Soc. A* **369**, 2087–2112 (2011).
21. Misra, A., Meadows, V., Claire, M. & Crisp, D. Using dimers to measure biosignatures and atmospheric pressure for terrestrial exoplanets. *Astrobiology* **14**, 67–86 (2014).
22. Gallagher, A. & Holstein, T. Collision-induced absorption in atomic electronic transitions. *Phys. Rev. A.* **16**, 2413 (1977).
23. Julienne, P. S. Non-adiabatic theory of collision-broadened atomic line profiles. *Phys. Rev. A.* **26**, 3299–3317 (1982).
24. Robinson, G. W. Intensity enhancement of forbidden electronic transitions by weak intermolecular interactions. *J. Chem. Phys.* **46**, 572 (1967).
25. Minaev, B. Intensities of spin-forbidden transitions in molecular oxygen and selective heavy-atom effects. *Int. J. Quantum Chem.* **17**, 367–374 (1980).
26. Minaev, B. F. & Ågren, H. Collision-induced $b^1\text{-}\ ^1\Sigma_g^-$ $a^1\Delta_g$, $b^1\Sigma_g^+$ -$X^3\Sigma_g^-$ and $a^1\Delta_g$-$X^3\Sigma_g^-$ transition probabilities in molecular oxygen. *J. Chem. Soc. Faraday Trans.* **93**, 2231–2239 (1997).
27. Minaev, B. F. & Kobzev, G. I. Response calculations of electronic and vibrational transitions in molecular oxygen induced by interaction with noble gases. *Spectrochim. Acta A* **59**, 3387–3410 (2003).
28. Minaev, B. F. Electronic mechanisms of molecular oxygen activation. *Russ. Chem. Rev.* **76**, 988–1010 (2007).
29. Long, C. & Kearns, D. R. Selection rules for the intermolecular enhancement of spin forbidden transitions in molecular oxygen. *J. Chem. Phys.* **59**, 5729 (1973).
30. Hidemori, T., Akai, N., Kawai, A. & Shibuya, K. Intensity enhancement of weak $O_2a^1\Delta_g - X^3$ emission at 1270 nm by collisions with foreign gases. *J. Phys. Chem. A* **116**, 2032 (2012).
31. Janssen, J. Analyse spectrale des éléments de l'atmosphère terrestre. *C. R. Acad. Sci.* **101**, 649–651 (1885).
32. Janssen, J. Sur les spectres d'absorption de l'oxygène. *C. R. Acad. Sci.* **102**, 1352 (1886).
33. Tabisz, G. C., Allin, E. J. & Welsh, H. L. Interpretation of the visible and near-infrared absorption spectra of compressed oxygen as collision-induced electronic transitions. *Can. J. Phys.* **47**, 2859–2871 (1969).
34. Greenblatt, G. D., Orlando, J. J., Burkhoder, J. B. & Ravishankara, A. R. Absorption measurements of oxygen between 330 and 1140 nm. *J. Geophys. Res.* **95**, 18577–18582 (1990).
35. Sneep, M., Ityaksov, D., Aben, I., Linnartz, H. & Ubachs, W. Temperature-dependent cross sections of O_2–O_2 collision-induced absorption resonances at 477 and 577 nm. *J. Quant. Spectrosc. Radiat. Transf.* **98**, 405–424 (2006).
36. Thalman, R. & Volkamer, R. Temperature dependent absorption cross-sections of O_2–O_2 collision pairs between 340 and 630 nm and at atmospherically relevant pressure. *Phys. Chem. Chem. Phys.* **15**, 15371–15381 (2013).
37. Karman, T., van der Avoird, A. & Groenenboom, G. C. Potential energy and dipole moment surfaces of the triplet states of the $O_2(X^3\Sigma_g^-)$–$O_2(X^3\Sigma_g^-, a^1\Delta_g, b^1\Sigma_g^+)$ complex. *J. Chem. Phys.* **147**, 084306 (2017).
38. Karman, T., van der Avoird, A. & Groenenboom, G. C. Communication: multiple-property-based diabatization for open-shell van der Waals molecules. *J. Chem. Phys.* **144**, 121101 (2016).
39. Zagidullin, M. V., Pershin, A. A., Azyazov, V. N. & Mebel, A. M. Luminescence of the $(O_2(a^1\Delta_g))_2$ collisional complex in the temperature range of 90–315 K: experiment and theory. *J. Chem. Phys.* **143**, 244315 (2015).
40. Karman, T., van der Avoird, A. & Groenenboom, G. C. Line-shape theory of the $X^3\Sigma_g^- \rightarrow a^1\Delta_g$, $b^1\Sigma_g^+$ transitions in O_2–O_2 collision-induced absorption. *J. Chem. Phys.* **147**, 084307 (2017).
41. Richard, C. et al. New section of the HITRAN database: collision-induced absorption (CIA). *J. Quant. Spectrosc. Radiat. Transf.* **113**, 1276–1285 (2012).
42. Gordon, I. E. et al. The HITRAN2016 molecular spectroscopic database. *J. Quant. Spectrosc. Radiat. Transf.* **203**, 3–69 (2017).
43. Olver, F. W. J., Lozier, D. W., Boisvert, R. F. & Clark, C. W. *The NIST Handbook of Mathematical Functions* (Cambridge Univ. Press, Cambridge, 2010).
44. Nichols, R. Franck–Condon factors to high vibrational quantum numbers V: O_2 band systems. *J. Res. Nat. Bur. Stand. A* **69A**, 369–373 (1965).
45. Drouin, B. J. et al. Multispectrum analysis of the oxygen A-band. *J. Quant. Spectrosc. Radiat. Transf.* **186**, 118–138 (2017).
46. Karman, T., Miliordos, E., Hunt, K. L. C., Groenenboom, G. C. & van der Avoird, A. Quantum mechanical calculation of the collision-induced absorption spectra of N_2–N_2 with anisotropic interactions. *J. Chem. Phys.* **142**, 084306 (2015).
47. Buryak, I., Lokshtanov, S. & Vigasin, A. CCSD(T) potential energy and induced dipole surfaces for N_2–$H_2(D_2)$: retrieval of the collision-induced absorption integrated intensities in the regions of the fundamental and first overtone vibrational transitions. *J. Chem. Phys.* **137**, 114308 (2012).
48. Moraldi, M. & Frommhold, L. Collision-induced infrared absorption by H_2–He complexes: accounting for the anisotropy of the interaction. *Phys. Rev. A* **52**, 274 (1995).

Acknowledgements

This work was funded by the Netherlands Organisation for Scientific Research (NWO; grant 022.003.048). T.K. acknowledges additional support by the EU COST Action MOLIM (CM1405) and a pre-doctoral fellowship of the Smithsonian Astrophysical Observatory. A.B. and D.H.P. acknowledge EU H2020 ITN-EID project 'PUFF' (grant no. 642820) for support. I.E.G. is supported by NASA AURA program grant NNX14AI55G.

Author contributions

The theory was developed by T.K., A.v.d.A. and G.C.G. Cavity ring-down experiments were performed M.A.J.K., A.B., D.H.P. and W.J.v.d.Z. I.E.G. contributed to the comparison between experiment and theory.

Competing interests

The authors declare no competing interests.

Additional information

Supplementary information is available for this paper at https://doi.org/10.1038/s41557-018-0015-x.

Reprints and permissions information is available at www.nature.com/reprints.

Correspondence and requests for materials should be addressed to G.C.G.

Publisher's note: Springer Nature remains neutral with regard to jurisdictional claims in published maps and institutional affiliations.

Supplementary Material:

$O_2 - O_2$ and $O_2 - N_2$ collision-induced absorption mechanisms unravelled

Tijs Karman,[1] Mark A. J. Koenis,[2] Agniva Banerjee,[1] David H. Parker,[1] Iouli E. Gordon,[3] Ad van der Avoird,[1] Wim J. van der Zande,[1] and Gerrit C. Groenenboom[1, a)]

[1)] *Institute for Molecules and Materials, Radboud University, Heyendaalseweg 135, 6525 AJ Nijmegen, the Netherlands*

[2)] *Van 't Hoff Institute for Molecular Sciences, University of Amsterdam, Science Park 904, 1098 XH, Amsterdam, The Netherlands*

[3)] *Harvard-Smithsonian Center for Astrophysics, 60 Garden street, Cambridge, MA 02138, USA*

(Dated: December 19, 2017)

[a)] Electronic mail: gerritg@theochem.ru.nl

CONTENTS

I. LINE-SHAPE CALCULATIONS

A. Formalism

This section sketches the theoretical formalism of the line-shape calculations used in this work. For an introduction as well as for a more extensive discussion and a derivation of the theoretical framework, the reader is referred to Ref.[1,2].

The collision-induced absorption coefficient at angular frequency ω and temperature T is given by

$$\alpha(\omega, T) = \frac{4\pi^2}{3\hbar c}\omega \left[1 - \exp\left(-\frac{\hbar\omega}{k_B T}\right)\right] V g(\omega, T), \tag{1}$$

with the spectral density in first-order perturbation theory

$$g(\omega, T) = \sum\!\!\!\!\!\!\int_i \sum\!\!\!\!\!\!\int_f P^{(i)}(T) |\langle f|\hat{\boldsymbol{\mu}}|i\rangle|^2 \delta(\omega_f - \omega_i - \omega). \tag{2}$$

In the above, $\hbar$ is the reduced Planck constant, c is the speed of light, V is the volume of the absorbing gas, and k_B is the Boltzmann constant. The states $|i\rangle$ and $|f\rangle$ represent the initial and final states, with energies $\hbar\omega_i$ and $\hbar\omega_f$, and $P^{(i)}(T)$ represents the thermal population of the initial state.

The formalism for evaluating Eqs. (1) and (2) consists of the following steps:

1. The states $|i\rangle$ and $|f\rangle$ are obtained from scattering calculations. For numerically exact results, this amounts to converged coupled-channels calculations.

2. The dipole overlap between these states, $\langle f|\hat{\boldsymbol{\mu}}|i\rangle$, is calculated.

3. The above is repeated for all states $|i\rangle$ and $|f\rangle$ required to accurately calculate the thermal average implied by Eq. (2), and for a sufficiently dense grid in the photon frequencies, ω.

The scattering calculations require diabatic potential energy surfaces for the ground and electronically-excited states, as well as diabatic transition dipole moment surfaces. These are obtained from *ab initio* electronic structure calculations, see Sec. I B.

It is useful to represent the orientation dependence of the diabatic potential energy and

dipole moment surfaces as the following angular expansions. For the potentials

$$\begin{aligned}\hat{V}(\boldsymbol{r}_A, \boldsymbol{r}_B, \boldsymbol{R}) = & \sum_{L_A, L_B, L} \mathcal{V}_{L_A, L_B, L}(r_A, r_B, R) \\ & \times \sum_{M_A, M_B, M} \langle L_A M_A L_B M_B | L M \rangle \langle L, M, L, \ -M | 00 \rangle \\ & \times D^{(L_A)*}_{M_A, K_A}(\boldsymbol{r}_A) D^{(L_B)*}_{M_B, K_B}(\boldsymbol{r}_B) C_{L, -M}(\boldsymbol{R}),\end{aligned} \tag{3}$$

and for the dipole moment surfaces

$$\begin{aligned}\hat{\mu}_\nu(\boldsymbol{r}_A, \boldsymbol{r}_B, \boldsymbol{R}) = & \sum_{L_A, L_B, \lambda, L} \mathcal{D}_{L_A, L_B, \lambda, L}(r_A, r_B, R) \\ & \times \sum_{M_A, M_B, \mu, M} \langle L_A M_A L_B M_B | \lambda \mu \rangle \langle \lambda \mu L M | 1 \nu \rangle \\ & \times D^{(L_A)*}_{M_A, K_A}(\boldsymbol{r}_A) D^{(L_B)*}_{M_B, K_B}(\boldsymbol{r}_B) C_{L, M}(\boldsymbol{R}).\end{aligned} \tag{4}$$

In the above, the vectors $\boldsymbol{r}_A$ and $\boldsymbol{r}_B$ denote the lengths and orientations of the monomer bonds, $\boldsymbol{R}$ denotes the intermolecular axis, $D^{(L)}_{M,K}(\boldsymbol{r})$ is a Wigner D-matrix element depending on the polar angles of the vector $\boldsymbol{r}$, with zyz Euler angles $(\phi, \theta, 0)$, similarly $C_{L,M}(\boldsymbol{R})$ is a Racah-normalized spherical harmonic, and $\langle j_1 m_1 j_2 m_2 | j_3 m_3 \rangle$ is a Clebsch-Gordan coefficient. The labels $\{L_A, L_B, \lambda, L\}$ enumerate the different angular components, and $\mathcal{V}_{L_A, L_B, L}(r_A, r_B, R)$ or $\mathcal{D}_{L_A, L_B, \lambda, L}(r_A, r_B, R)$ are the corresponding expansion coefficients that, in general, depend on the monomer bond lengths r_A, r_B, and the intermolecular distance, R. For brevity of notation, we have suppressed the dependence on the diabatic electronic states involved, which also determines the value of K_A and K_B, symmetry restrictions, and the ranges of L_A, L_B, λ and L. The reader is referred to Ref.[1,2] for more details.

To the best of our knowledge, numerically exact line-shape calculations for bi-molecular collisions as sketched above have only been performed for $H_2 - H_2$.[3,4] For heavier diatomic molecules, the coupled-channels calculations at energies required to calculate thermal averages at any temperature of interest rapidly become prohibitively expensive. The roto-translational spectra of $N_2 - N_2$ have been calculated in a helicity-decoupling or coupled-states approximation,[5] but otherwise spectra have been computed either using classical formalisms,[6,7] or using the isotropic interaction approximation.[8]

To the best of our knowledge, line-shape calculations for electronic transitions in bi-molecular collisions have not before been attempted. We note that in an accurate coupled-

channels treatment of electronic excitations in $O_2 - O_2$, the degeneracy of the excited electronic states further increases the computational cost. For transitions to $O_2(a^1\Delta_g) + O_2(X^3\Sigma_g^-)$ and $O_2(b^1\Sigma_g^+) + O_2(X^3\Sigma_g^-)$, this degeneracy increases the dimension of the channel basis four-fold and two-fold, respectively. Combined with the N^3 scaling of the computational effort of coupled-channels calculations, where N is the dimension of the basis set, this leads to 64 and 8-fold increases in computational cost, compared to calculations for roto-translational spectra. Therefore, we restrict ourselves to calculations in the isotropic interaction approximation, which is commonly used for roto-translational and vibrational transitions.[8]

In the isotropic interaction approximation, the potential is replaced by its angular average. This is accomplished by removing all terms with $L_X > 0$, $X = A, B$, from Eq. (3). No approximation to the dipole surface of Eq. (4) is made. In this approximation, the radial and angular degrees of freedom are separable, such that the scattering wavefunction can be written as the product of roto-vibronic monomer wavefunctions for both molecules, $|\psi_A\rangle$ and $|\psi_B\rangle$, and angular momentum ket $|\ell m_\ell\rangle$ describing the end-over-end rotation, and a radial wavefunction, $U_\ell^{\psi_A,\psi_B}(R)$,

$$|i\rangle, |f\rangle \rightarrow |\psi_A\rangle|\psi_B\rangle|\ell m_\ell\rangle U_\ell^{\psi_A,\psi_B}(R). \tag{5}$$

The radial wavefunction is calculated numerically in computationally-inexpensive single-channel scattering calculations. The angular degrees of freedom can be treated analytically, as is shown in Ref.[2] where we have generalized this theory to treat electronic transitions.

This leads to expressions for the spectral density of the following form

$$\begin{aligned} Vg(\omega) = & \sum_{L_A,L_B,\lambda,L} \sum_{N_A,N_B,N'_A,N'_B} P_{N_A} P_{N_B} \frac{(1)(N_A)(N'_A)(N_B)(N'_B)}{(L_A)(L_B)(L)} \\ & \times \begin{pmatrix} N_A & L_A & N'_A \\ \Lambda_A & K_A & -\Lambda'_A \end{pmatrix}^2 \begin{pmatrix} N_B & L_B & N'_B \\ \Lambda_B & K_B & -\Lambda'_B \end{pmatrix}^2 VG_{L_A,L_B,\lambda,L}(\omega - \omega_0 - \omega_{\rm rot}), \end{aligned} \tag{6}$$

where the quantity in round brackets is a Wigner 3-jm symbol, the short-hand notation $(j) = 2j + 1$, and $VG(\omega)$ is a translational profile, which is discussed below. We note that, again, the notation for the diabatic electronic states is implicit. Equation (6) is further modified depending on the degeneracy and symmetry of the initial and final states, and depending on the underlying absorption mechanism, see Ref.[2] for a detailed discussion.

From Eq. (6), we observe that the spectrum is given by an incoherent superposition of contributions of different angular components $\{L_A, L_B, \lambda, L\}$. Each of these contributions consists of a set of rotational transitions, the intensity of which is controlled by the population of rotational levels, P_{N_X}, and the by the 3-jm symbols in Eq. (6). Superimposed on these rotational transitions is a translational profile, which is defined by

$$VG_{L_A,L_B,\lambda,L}(\omega) = \hbar\lambda_0^3 \sum_{\ell,\ell'} (\ell)(\ell') \begin{pmatrix} \ell & L & \ell' \\ 0 & 0 & 0 \end{pmatrix}^2 \times \int_0^\infty dE_{\rm col} \exp\left(-\frac{E_{\rm col}}{k_B T}\right) |\langle \ell E_{\rm col}|\mathcal{D}_{L_A,L_B,\lambda,L}(R)|\ell', E_{\rm col} + \hbar\omega\rangle|^2, \qquad (7)$$

where $\lambda_0 = \hbar\sqrt{\frac{2\pi}{\mu k_B T}}$ is the thermal de Broglie wave length, and $|\ell, E_{\rm col}\rangle$ are scattering wavefunctions for kinetic energy $E_{\rm col}$ and partial wave quantum number ℓ. The translational profiles are typically much broader than the underlying rotational structure.

B. Transition dipole and potential energy surfaces

The line-shape calculations require knowledge of the transition dipole moment and potential energy as a function of the nuclear coordinates, known as dipole and potential energy surfaces. The potential energy surfaces for ground and excited triplet states of $O_2 - O_2$, and the intermolecular-exchange-induced transition dipole surfaces are taken from Ref.[1]. For the spin-orbit based mechanism, we use the long-range model proposed in Ref.[2]. For completeness, section I C reviews this model, and also discusses spin-orbit-induced magnetic dipole and electric quadrupole monomer transitions.

Isotropic potentials are used in all line-shape calculations. The triplet $O_2 - O_2$ potentials are taken from Ref.[1]. We also use these potentials for the singlet and quintet states of $O_2 - O_2$, and even for $O_2 - N_2$. Ground state $O_2 - N_2$ potentials,[9] and spin-dependent $O_2 - O_2$ potentials are available in the literature,[10] but potentials for the excited states of $O_2 - N_2$ are not. However these approximations should be accurate, as the differences between the employed *isotropic parts* of these potentials are relatively small. Furthermore, the differences between the isotropic potentials are small compared to the differences due to orientation dependence of the potential, which are neglected.

C. Spin-orbit coupling in O_2

The theory of spin-orbit coupling in the O_2 molecule has been pioneered by Minaev and co-workers[11,12]. The spin-orbit interaction mixes the $X^3\Sigma_g^-$ and $b^1\Sigma_g^+$ states

$$\begin{aligned} |\Psi_{X,0}\rangle =& |X^3\Sigma_g^-\rangle + C_{\mathrm{SO}}|b^1\Sigma_g^+\rangle, \\ |\Psi_b\rangle =& |b^1\Sigma_g^+\rangle - C_{\mathrm{SO}}^*|X^3\Sigma_g^-\rangle, \end{aligned} \tag{8}$$

where the mixing constant can be evaluated using first-order perturbation theory[12]

$$C_{\mathrm{SO}} = \frac{\langle b^1\Sigma_g^+|\hat{H}_{\mathrm{SO}}|X^3\Sigma_g^-\rangle}{E_X - E_b} = 0.0134i. \tag{9}$$

There is no spin-orbit coupling between the $a^1\Delta_g$ and either of the other states considered here. The mixing between the triplet ground state and singlet excited state breaks the spin symmetry. This leads to magnetic dipole moments for the $X^3\Sigma_g^- \to b^1\Sigma_g^+$ transition, and electric quadrupole moments for both $X^3\Sigma_g^- \to a^1\Delta_g$ and $X^3\Sigma_g^- \to b^1\Sigma_g^+$ transitions, the latter are given by

$$\langle a^1\Delta_g|\hat{\Theta}_2|\Psi_{X,0}\rangle = C_{\mathrm{SO}}\langle a^1\Delta_g|\hat{\Theta}_2|b^1\Sigma_g^+\rangle, \tag{10a}$$

$$\langle \Psi_b|\hat{\Theta}_0|\Psi_{X,0}\rangle = C_{\mathrm{SO}}\left[\langle b^1\Sigma_g^+|\hat{\Theta}_0|b^1\Sigma_g^+\rangle - \langle X^3\Sigma_g^-|\hat{\Theta}_0|X^3\Sigma_g^-\rangle\right]. \tag{10b}$$

Here, the quadrupole operator is defined as

$$\Theta_K = \sum_i q_i r_i^2 C_{2,K}(\boldsymbol{r}_i), \tag{11}$$

where the sum extends over all electrons and nuclei with charge q_i and position $\boldsymbol{r}_i$. Both the magnetic dipole and electric quadrupole moments give rise to observable monomer absorption lines,[13,14] but the electric quadrupole transitions are much weaker.

It is worth noting the difference between the strengths of the $X^3\Sigma_g^- \to a^1\Delta_g$ and $X^3\Sigma_g^- \to b^1\Sigma_g^+$ transitions. Magnetic dipole moments are stronger for the $X^3\Sigma_g^- \to b^1\Sigma_g^+$ transition because these states are spin-orbit coupled directly, and the transition borrows intensity from the ground-state spin current. Magnetic dipole moments for the $X^3\Sigma_g^- \to a^1\Delta_g$ transition are non-zero only due to spin-orbit coupling to intermediate $^1\Pi$ and $^3\Pi$ states. This coupling is less effective, and the magnetic dipole moments are an order of magnitude smaller. For the electric quadrupole transitions, the situation is reversed. Taking into account spin-orbit coupling between the $X^3\Sigma_g^-$ and $b^1\Sigma_g^+$ states, the $X^3\Sigma_g^- \to a^1\Delta_g$ transition borrows intensity

from the strong Noxon quadrupole moment, whereas the $X^3\Sigma_g^- \to b^1\Sigma_g^+$ quadrupole moment is proportional to the *difference* in ground and excited state quadrupole moment, and hence is much smaller. In fact, this quadrupole moment is so small that the contribution of $^1\Pi$ and $^3\Pi$ intermediate states becomes important, see Eq. (12). This does not change the conclusion that magnetic dipole transitions are stronger for $X^3\Sigma_g^- \to b^1\Sigma_g^+$, whereas electric quadrupole transitions are stronger for $X^3\Sigma_g^- \to a^1\Delta_g$.

Here, the transition quadrupole moment is relevant, not due to the weak monomer quadrupole transitions, but rather as it gives rise to an induced transition dipole moment in collision complexes through quadrupole induction. In this first-order long-range model, the transition dipole moment is given in terms of the spin-orbit-induced transition quadrupole moment,

$$\begin{aligned}
\langle X^3\Sigma_g^-, \Omega | \Theta_{\Omega-\Omega'} | a^1\Delta_g, \Omega' \rangle &= \begin{cases} 0.0134i & \text{for } \Omega = 0, \\ 0 & \text{for } |\Omega| = 1, \end{cases} \\
\langle X^3\Sigma_g^-, \Omega | \Theta_{\Omega-\Omega'} | b^1\Sigma_g^+, \Omega' \rangle &= \begin{cases} 0.0021i & \text{for } \Omega = 0, \\ 0.0050i & \text{for } |\Omega| = 1, \end{cases}
\end{aligned} \tag{12}$$

and the isotropic polarizability of the perturber, α_0. In the above, $\Omega = \Lambda + \Sigma$ is the bond axis projection of the total angular momentum. The angular dependence, and the R^{-4} radial dependence are then known analytically from first-order electrostatic long-range theory. This is given by a single term of Eq. (4), given by

$$\mathcal{D}^{(\mathrm{SO})}_{2,0,2,3}(r_A, r_B, R) = \sqrt{35}\ \Theta^{(A)}_{\Omega_A - \Omega'_A}(r_A)\ \alpha_0^{(B)}(r_B)\ R^{-4}. \tag{13}$$

This spin-orbit mechanism also applies to O_2-N_2 collisions, where the isotropic polarizability of O_2, $\alpha_0 = 10.87\ a_0^3$, is to be replaced by $11.74\ a_0^3$ for N_2.[15]

A second contribution to the induced dipole moment could be the polarization of a spin-orbit perturbed O_2 molecule in the electric field of the permanent quadrupole moment of the perturber. This also corresponds to first-order quadrupole induction, but involves the permanent quadrupole moment of the perturber and the spin-orbit-induced transition polarizability of the absorbing O_2 molecule. For the $X^3\Sigma_g^- \to b^1\Sigma_g^+$ transition, including only spin-orbit coupling between these states, the isotropic transition polarizability is given by the difference in ground and excited state polarizability

$$\langle \Psi_b | \hat{\alpha}_0 | \Psi_{X,0} \rangle = C_{\mathrm{SO}} \left[\langle b^1\Sigma_g^+ | \hat{\alpha}_0 | b^1\Sigma_g^+ \rangle - \langle X^3\Sigma_g^- | \hat{\alpha}_0 | X^3\Sigma_g^- \rangle \right]. \tag{14}$$

We estimate the polarizabilities from simple multi-reference configuration interaction (MRCI) calculations as 10.2 a_0^3 and 9.48 a_0^3 for the $X^3\Sigma_g^-$ and $b^1\Sigma_g^+$ states, respectively. The ground state polarizability is in good agreement with the literature value of 10.87 a_0^3 from Ref.[15]. We thus expect the $X^3\Sigma_g^- \rightarrow b^1\Sigma_g^+$ transition polarizability to be in the order of $0.7\, C_{\mathrm{SO}} = 0.009i$ atomic units. We estimate the contribution of the transition polarizability from the products with the permanent quadrupole moment, which is $-0.264\ ea_0^2$ or $-1.052\ ea_0^2$ for O_2 or N_2, respectively. This is compared to the product of transition quadrupole moment and permanent polarizability, considered in the previous paragraph. Even for the $O_2 - N_2$ case, where the perturbing quadrupole moment is strongest, we find that the contribution of the transition polarizability to the intensity – which is proportional to the square of the dipole moment – is two orders of magnitude weaker. It should be noted that this is strongly dependent on the exact transition polarizability, which is only estimated here. Summarizingly, the contribution of the transition polarizability is expected to be small. We neglect this contribution, which furthermore does not impact the predicted line shape, as this contribution has a similar angular dependence and identical R^{-4} radial dependence. For the $X^3\Sigma_g^- \rightarrow a^1\Delta_g$ transition, there is no estimate of the relevant $b^1\Sigma_g^+ \rightarrow a^1\Delta_g$ transition polarizability available, but we expect the contribution of the transition polarizability to be even less significant as the $X^3\Sigma_g^- \rightarrow a^1\Delta_g$ transition quadrupole moment is much larger.

D. Vibrational transitions

In this work, we consider various vibronic bands of O_2. The different vibronic transitions which underly each band are given in Table I. For the $O_2 - N_2$ system, the vibrational transition necessarily occurs on the O_2 molecule, or it would contribute to a different frequency region. For $O_2 - O_2$, the vibrational transitions can occur on the molecule undergoing the electronic transition, on the perturbing molecule, or on both. The electronic states involved have vibrational frequencies which differ by less than the typical width of a vibronic band, such that vibrational transitions contribute to the same frequency band irrespective of whether the vibrational transition occurs on the molecule undergoing electronic excitation, or on the collision partner.

To *ab initio* compute the absorption for a vibronic transition, rather than $v'' = 0 \rightarrow v' = 0$, the dipole expansion coefficient in Eq. (7) should be replaced by the relevant vibrational

Table I. This table shows the different processes which contribute to each vibronic band, as schematically indicated by $v' = 0, 1, 2$. The table is limited to the $b^1\Sigma_g^+$ excited electronic state, but also applies to the $a^1\Delta_g$ state, where additionally a sum over the two spatially degenerate components of the electronic state is implied.

System	Band	Final states
$O_2 - N_2$	$X^3\Sigma_g^- \rightarrow b^1\Sigma_g^+ \, (v' = 0)$	$O_2 \left[b^1\Sigma_g^+ \, (v' = 0)\right] + N_2 \left[X^1\Sigma_g^+ \, (v' = 0)\right]$
	$X^3\Sigma_g^- \rightarrow b^1\Sigma_g^+ \, (v' = 1)$	$O_2 \left[b^1\Sigma_g^+ \, (v' = 1)\right] + N_2 \left[X^1\Sigma_g^+ \, (v' = 0)\right]$
	$X^3\Sigma_g^- \rightarrow b^1\Sigma_g^+ \, (v' = 2)$	$O_2 \left[b^1\Sigma_g^+ \, (v' = 2)\right] + N_2 \left[X^1\Sigma_g^+ \, (v' = 0)\right]$
$O_2 - O_2$	$X^3\Sigma_g^- \rightarrow b^1\Sigma_g^+ \, (v' = 0)$	$O_2^{(A)} \left[b^1\Sigma_g^+ \, (v' = 0)\right] + O_2^{(B)} \left[X^3\Sigma_g^- \, (v' = 0)\right]$
		$O_2^{(A)} \left[X^3\Sigma_g^- \, (v' = 0)\right] + O_2^{(B)} \left[b^1\Sigma_g^+ \, (v' = 0)\right]$
$O_2 - O_2$	$X^3\Sigma_g^- \rightarrow b^1\Sigma_g^+ \, (v' = 1)$	$O_2^{(A)} \left[b^1\Sigma_g^+ \, (v' = 1)\right] + O_2^{(B)} \left[X^3\Sigma_g^- \, (v' = 0)\right]$
		$O_2^{(A)} \left[X^3\Sigma_g^- \, (v' = 1)\right] + O_2^{(B)} \left[b^1\Sigma_g^+ \, (v' = 0)\right]$
		$O_2^{(A)} \left[b^1\Sigma_g^+ \, (v' = 0)\right] + O_2^{(B)} \left[X^3\Sigma_g^- \, (v' = 1)\right]$
		$O_2^{(A)} \left[X^3\Sigma_g^- \, (v' = 0)\right] + O_2^{(B)} \left[b^1\Sigma_g^+ \, (v' = 1)\right]$
$O_2 - O_2$	$X^3\Sigma_g^- \rightarrow b^1\Sigma_g^+ \, (v' = 2)$	$O_2^{(A)} \left[b^1\Sigma_g^+ \, (v' = 2)\right] + O_2^{(B)} \left[X^3\Sigma_g^- \, (v' = 0)\right]$
		$O_2^{(A)} \left[X^3\Sigma_g^- \, (v' = 2)\right] + O_2^{(B)} \left[b^1\Sigma_g^+ \, (v' = 0)\right]$
		$O_2^{(A)} \left[b^1\Sigma_g^+ \, (v' = 0)\right] + O_2^{(B)} \left[X^3\Sigma_g^- \, (v' = 2)\right]$
		$O_2^{(A)} \left[X^3\Sigma_g^- \, (v' = 0)\right] + O_2^{(B)} \left[b^1\Sigma_g^+ \, (v' = 2)\right]$
		$O_2^{(A)} \left[b^1\Sigma_g^+ \, (v' = 1)\right] + O_2^{(B)} \left[X^3\Sigma_g^- \, (v' = 1)\right]$
		$O_2^{(A)} \left[X^3\Sigma_g^- \, (v' = 1)\right] + O_2^{(B)} \left[b^1\Sigma_g^+ \, (v' = 1)\right]$

matrix element, that is

$$\mathcal{D}_{L_A,L_B,\lambda,L}(R) \rightarrow \int\int \psi^*_{v''_A}(r_A)\psi^*_{v''_B}(r_B)\mathcal{D}_{L_A,L_B,\lambda,L}(r_A, r_B, R)\psi_{v'_A}(r_A)\psi_{v'_B}(r_B) \; r_A^2 dr_A \; r_B^2 dr_B, \tag{15}$$

where $\psi_v(r)$ is a monomer vibrational wavefunction. Transition dipole surfaces for the exchange based mechanism that include monomer vibrational coordinates are unavailable and we do not explicitly include the monomer vibration. We assume that different vibrational

bands are related by a scaling factor, that is, the intensity is affected but the line shape is not. This should be reasonable as the line shape is determined by the length scale of the exponential R-dependence of $\mathcal{D}$, as shown in Sec. I E, which should be less strongly dependent on the vibrational coordinates, r_A and r_B.

For the spin-orbit mechanism, the dipole surface is given in terms of monomer transition quadrupole moments and polarizabilities, and vibrational matrix elements are given in terms of vibrational transition moments of these monomer properties,

$$\int\int \psi^*_{v''_A}(r_A)\psi^*_{v''_B}(r_B)\ \mathcal{D}^{(\mathrm{SO})}_{2,0,2,3}(r_A,r_B,R)\ \psi_{v'_A}(r_A)\psi_{v'_B}(r_B)\ r_A^2 dr_A\ r_B^2 dr_B = \sqrt{35}\ R^{-4}\left[\int \psi^*_{v''_A}(r_A)\Theta^{(A)}(r_A)\psi_{v'_A}(r_A)r_A^2 dr_A\right]\left[\int \psi^*_{v''_B}(r_B)\alpha_0^{(B)}(r_B)\psi_{v'_B}(r_B)r_B^2 dr_B\right]. \tag{16}$$

We note that this implies – as is assumed above for the exchange mechanism – the intensity of vibrational transitions is modified, but the R^{-4} radial dependence, and therefore the absorption line shape, is unaffected. For $O_2 - N_2$, the vibrational transition occurs on the O_2 molecule, monomer A, such that $v''_B = v'_B = 0$. Thus, the intensity of $O_2 - N_2$ vibronic transitions is determined completely by the v'-dependence of the O_2 transition quadrupole moment. Because the transition quadrupole moment weakly depends on the vibration coordinate, the intensity is reduced by approximately a Franck-Condon factor. These are tabulated in Ref.[16] for the O_2 transitions studied here, and range from 10^{-4} to $7 \cdot 10^{-2}$. The Franck-Condon factors are unfavorable since ground and excited states correspond to the same electronic configuration, and hence have very similar potential energy curves.

E. Analytical line-shape model

Here, we present a qualitative model that offers insight into the absorption line shape and its dependence on the underlying absorption mechanism. The absorption spectrum, in the isotropic interaction approximation, can be understood as a superposition of translational profiles centered at each rotational transition. The angular dependence of the dipole surface determines the intensity of the rotational transitions, whereas the radial dependence determines the translational profile, given by Eq. (7) The translational profile is typically broader than the rotational structure, such that it largely determines absorption line shape.

In order to derive simple analytical expressions for the translational profile, we assume that the radial wavefunctions are independent of the relative angular momentum, ℓ, and describe scattering on a hard-sphere potential. In this approximation, the energy-normalized radial wavefunction is given by

$$\langle R|\ell E_{\rm col}\rangle = \begin{cases} \frac{1}{\hbar R}\sqrt{\frac{\mu}{2\pi k}}\sin\left[k\left(R-a\right)\right] & \text{for } R \geq a, \\ 0 & \text{for } R < a, \end{cases} \tag{17}$$

where a is the hard-sphere radius, μ is the reduced mass, and the wave number, k, satisfies $\hbar k = \sqrt{2\mu E_{\rm col}}$. We further assume that the thermal averaging can be approximated by simply setting the kinetic energy $E_{\rm col} = k_B T$, such that the translational profile becomes

$$\begin{aligned} VG(\omega) &\propto \frac{1}{kk'}\left|\int_a^\infty \sin\left[k\left(R-a\right)\right]\sin\left[k'\left(R-a\right)\right]\mathcal{D}(R)dR\right|^2 \\ &= \frac{1}{kk'}\left|\int_0^\infty \sin(kR)\sin(k'R)\mathcal{D}(R+a)dR\right|^2. \end{aligned} \tag{18}$$

The frequency dependence is contained in the final wave number, as $\hbar k' = \sqrt{2\mu(k_B T + \hbar\omega)}$. The translational profile is related to the Fourier transform of the dipole surface, as can be seen from Eq. (18). This qualitatively means that for short-ranged dipole surfaces, we will obtain broad absorption features, whereas for long-ranged dipole surfaces, the absorption feature will be narrower. In what follows, we will make this argument more quantitative, by evaluating Eq. (18) explicitly for the short-ranged exchange mechanism, $\mathcal{D} \propto \exp(-\gamma R)$, and the long-ranged spin-orbit mechanism, $\mathcal{D} \propto R^{-4}$.

For the exchange mechanism, we require only the Fourier transform of an exponentially decaying function, which is a Lorentzian. This yields the translational profile

$$VG_{\rm exchange} \propto \frac{\gamma^2\sqrt{k_B T(k_B T + \hbar\omega)}}{\left\{(\gamma^2 + 2\mu k_B T)^2 + 4\mu(\gamma^2 - 2\mu k_B T)(k_B T + \hbar\omega) + \left[2\mu\left(k_B T + \hbar\omega\right)\right]^2\right\}^2}, \tag{19}$$

where γ is the length scale of the dipole surface, $\mathcal{D} \propto \exp(-\gamma R)$. The width of the profile increases with γ, *i.e.*, as the dipole surface becomes more short ranged.

For the spin-orbit mechanism, $\mathcal{D} \propto R^{-4}$, and we require the integral

$$\begin{aligned} \int_0^\infty \sin(kR)\sin(k'R)(R+a)^{-4}dR =& \frac{1}{2}\int_0^\infty \cos[(k+k')R](R+a)^{-4}dR \\ &- \frac{1}{2}\int_0^\infty \cos[(k-k')R](R+a)^{-4}dR. \end{aligned} \tag{20}$$

We neglect the first term on the right-hand side, which is an integral of a more rapidly oscillatory function, and obtain for the second term

$$\int_0^\infty \cos[(k-k')R](R+a)^{-4}dR \propto G_{1,3}^{3,1}\left(\frac{a^2}{4}(k-k')^2 \,\middle|\, \begin{matrix} 0 \\ 0 \;\; \frac{3}{2} \;\; 2 \end{matrix}\right), \tag{21}$$

where $G_{1,3}^{3,1}$ is a Meijer G function.[17] For the translational profile, this yields

$$VG_{\mathrm{spin-orbit}} \propto \frac{1}{kk'}\left[G_{1,3}^{3,1}\left(\frac{\mu a^2}{2}\left[\sqrt{k_BT}-\sqrt{k_BT+\hbar\omega}\right]^2 \,\middle|\, \begin{matrix} 0 \\ 0 \;\; \frac{3}{2} \;\; 2 \end{matrix}\right)\right]^2. \tag{22}$$

In Fig. 3 of the main text, these model translational profiles are evaluated numerically and compared to results of the full line-shape calculations. For comparison, we have selected the $\{L_A, L_B, \lambda, L\} = \{4, 0, 4, 5\}$ angular contribution to the exchange mechanism for $X^3\Sigma_g^- \rightarrow a^1\Delta_g$, using the MRCI dipole surface, which contributes 28 % of the intensity. For the spin-orbit mechanism, we compare the only contributing angular term corresponding to $\{L_A, L_B, \lambda, L\} = \{2, 0, 2, 3\}$. In numerically evaluating the model line shapes, we have used the parameters $\gamma = 3\ a_0^{-1}$ and $a = 7\ a_0$. All results correspond to room temperature. The model line shapes have been scaled vertically to match the observed intensity. The observed match of the profile's width confirms – and makes more quantitative – the argument that long-ranged (short-ranged) dipole surfaces lead to absorption on long (short) time-scales and hence result in narrow (broad) absorption features. This explains the observed qualitative differences in the absorption line shapes between the two mechanisms.

F. Computational details

We performed quantum mechanical line shape calculations using the theory presented in Ref.[2]. This involves calculating single-channel scattering wavefunctions for elastic scattering on the isotropic potentials of Ref.[1]. These calculations were performed using the renormalized Numerov algorithm,[18] for all partial waves $\ell < 150$, on discrete grids in the collision energy. The energy grid ranged from 0.1 K to 3000 K, with 75 logarithmically spaced points. Additional energies were included above and below each resonance, such that the non-resonant background is sampled, rather than the unphysically narrow resonances associated with the isotropic interaction approximation. A discrete equidistant grid in the radial coordinate was used, from R=4.5 to 30 a_0 in steps of 0.017 a_0.

From these single-channel scattering wavefunction, we have computed the overlap with the radial expansion coefficients of the transition dipole surfaces. We used spline interpolation of the logarithm of the squared overlap, followed by exponentiation, to interpolate the squared dipole overlap. This allowed us to evaluate the squared dipole overlap on discrete grids in the initial kinetic energy, E, and kinetic energy difference, $\omega = E' - E$, rather than initial and final kinetic energy, E and E'. Thermal averaging of the translational profile was subsequently performed by integrating the interpolated squared dipole overlap, multiplied by a Boltzmann factor, over the initial collision energy using a trapezoidal quadrature rule. From the numerically evaluated translational profile, the absorption spectrum is obtained using analytical equations such as Eq. (6).[2]

G. Detailed balance

The spectral density, Eq. (2), repeated here for clarity,

$$g(\omega, T) = \sum\!\!\!\!\!\!\int_i \sum\!\!\!\!\!\!\int_f P^{(i)}(T) |\langle f|\hat{\boldsymbol{\mu}}|i\rangle|^2 \delta(\omega_f - \omega_i - \omega), \tag{23}$$

possesses symmetry with respect to the interchange of the roles of the initial and final states, and sign reversal of the angular frequency. To be explicit, we have

$$\begin{aligned} g(-\omega, T) &= \sum\!\!\!\!\!\!\int_i \sum\!\!\!\!\!\!\int_f P^{(f)}(T) \exp\left(\frac{E_f - E_i}{kT}\right) |\langle f|\hat{\boldsymbol{\mu}}|i\rangle|^2 \delta(\omega_f - \omega_i + \omega) \\ &= \exp\left(-\frac{\hbar\omega}{kT}\right) \sum\!\!\!\!\!\!\int_i \sum\!\!\!\!\!\!\int_f P^{(f)}(T) |\langle f|\hat{\boldsymbol{\mu}}|i\rangle|^2 \delta(-\omega_f + \omega_i - \omega) \\ &= \exp\left(-\frac{\hbar\omega}{kT}\right) \sum\!\!\!\!\!\!\int_i \sum\!\!\!\!\!\!\int_f P^{(i)}(T) |\langle i|\hat{\boldsymbol{\mu}}|f\rangle|^2 \delta(-\omega_i + \omega_f - \omega) \\ &= \exp\left(-\frac{\hbar\omega}{kT}\right) g(\omega, T). \end{aligned} \tag{24}$$

Where, in the first step, we used the definition of the spectral density, and the relation between initial and final state populations

$$P^{(i)}(T) = P^{(f)}(T) \exp\left(\frac{E_f - E_i}{kT}\right). \tag{25}$$

In the second step, we use that the δ-function selects a single value of $\omega = \omega_i - \omega_f$, and that the δ-function is symmetric, $\delta(-x) = \delta(x)$. In the third step, we simply interchange

the dummy integration labels i and f, and finally recognize the definition of the spectral density.

The above result for the spectral density

$$g(-\omega, T) = \exp\left(-\frac{\hbar\omega}{kT}\right) g(\omega, T), \tag{26}$$

represents a rigorous detailed balance relation between collision-induced absorption and emission. Further approximate detailed balance relations can be derived which relate positive and negative *detuning*, $\Delta\omega$, with respect to a specific vibronic transition at frequency ω_0, rather than positive and negative absolute frequency, $\omega = \omega_0 + \Delta\omega$. We consider the case where the detuning is small compared to the absolute frequency, $|\Delta\omega| \ll \omega_0$, such that we can consider the frequency dependent factors in the definition of the absorption coefficient, Eq. (1), to be constant, and derive approximate detailed balance relations for the spectral density, Vg, Eq. (2), and translational profile, VG, Eq. (7).

The translational profiles are of the form of Eq. (7), which is restricted to free-to-free transitions for simplicity. At negative frequency we obtain

$$\begin{aligned}
VG_{L_A,L_B,\lambda,L}(-\omega_{\rm trans}) &= \hbar\lambda_0^3 \sum_{\ell,\ell'} (\ell)(\ell') \begin{pmatrix} \ell & L & \ell' \\ 0 & 0 & 0 \end{pmatrix}^2 \\
&\times \int_0^\infty dE_{\rm col} \exp\left(-\frac{E_{\rm col}}{k_B T}\right) |\langle \ell E_{\rm col} | \mathcal{D}_{L_A,L_B,\lambda,L}(R) | \ell', E_{\rm col} - \hbar\omega_{\rm trans}\rangle|^2, \\
&= \hbar\lambda_0^3 \sum_{\ell,\ell'} (\ell)(\ell') \begin{pmatrix} \ell & L & \ell' \\ 0 & 0 & 0 \end{pmatrix}^2 \\
&\times \int_{\hbar\omega_{\rm trans}}^\infty dE_{\rm col} \exp\left(-\frac{E_{\rm col}}{k_B T}\right) |\langle \ell E_{\rm col} | \mathcal{D}_{L_A,L_B,\lambda,L}(R) | \ell', E_{\rm col} - \hbar\omega_{\rm trans}\rangle|^2, \\
&= \hbar\lambda_0^3 \sum_{\ell,\ell'} (\ell)(\ell') \begin{pmatrix} \ell & L & \ell' \\ 0 & 0 & 0 \end{pmatrix}^2 \\
&\times \int_0^\infty dE_{\rm col} \exp\left(-\frac{E_{\rm col} + \hbar\omega_{\rm trans}}{k_B T}\right) |\langle \ell', E_{\rm col} + \hbar\omega_{\rm trans} | \mathcal{D}_{L_A,L_B,\lambda,L}(R) | \ell E_{\rm col}\rangle|^2, \\
&\approx \exp\left(-\frac{\hbar\omega_{\rm trans}}{k_B T}\right) VG_{L_A,L_B,\lambda,L}(\omega_{\rm trans}).
\end{aligned} \tag{27}$$

The derivation is similar to what is presented above for the spectral density for collision-induced emission. The first step is simply the definition of the translational profile, evaluated at negative frequency. In the second step, the lower limit on the integration is modified to

exclude the region where $E_{\rm col} - \hbar\omega_{\rm trans} < 0$, which does not contribute as the density of free-state wave functions vanishes. In the third step, the integration variable is substituted and the summation labels ℓ and ℓ' are interchanged. Assuming that

$$|\langle \ell', E_{\rm col} + \hbar\omega_{\rm trans}|\mathcal{D}_{L_A,L_B,\lambda,L}(R)|\ell E_{\rm col}\rangle|^2 \approx |\langle \ell E_{\rm col}|\mathcal{D}_{L_A,L_B,\lambda,L}(R)|\ell', E_{\rm col} + \hbar\omega_{\rm trans}\rangle|^2, \quad (28)$$

we then recognize the definition of the translational profile in the last step. Equation (28) appears to be rigorous, in the short-hand notation employed here, but is approximate as the bra-states are understood to be initial state translational wavefunctions, and ket-states are understood to be final state translational wavefunctions. A more faithful notation may be

$$\begin{aligned}|\langle {\rm initial}, \ell', E_{\rm col} + \hbar\omega_{\rm trans}|\mathcal{D}_{L_A,L_B,\lambda,L}(R)|{\rm final}, \ell, E_{\rm col}\rangle|^2 \approx \\ |\langle {\rm initial}, \ell, E_{\rm col}|\mathcal{D}_{L_A,L_B,\lambda,L}(R)|{\rm final}, \ell', E_{\rm col} + \hbar\omega_{\rm trans}\rangle|^2, \end{aligned} \quad (29)$$

or more compactly

$$|{\rm initial}, \ell, E_{\rm col}\rangle \approx |{\rm final}, \ell, E_{\rm col}\rangle. \quad (30)$$

This relation is not exact as the initial and final states correspond to different electronic states, and hence the translational wavefunctions are solutions to Schrödinger equations involving different potentials. However, since all electronic states involved correspond to the same configuration, and hence the involved potentials are very similar, the above represents a reasonable approximation. In summary, this leads to

$$VG_{L_A,L_B,\lambda,L}(-\omega_{\rm trans}) \approx \exp\left(-\frac{\hbar\omega_{\rm trans}}{k_B T}\right) VG_{L_A,L_B,\lambda,L}(\omega_{\rm trans}), \quad (31)$$

an approximate detailed balance relation for the translational profile.

We now turn our attention to approximate detailed balance relations for the spectral density, which is of the form of Eq. (6), repeated here in terms of the detuning, $\Delta\omega$,

$$\begin{aligned}Vg(\omega_0 + \Delta\omega) = \sum_{L_A,L_B,\lambda,L} \sum_{N_A,N_B,N'_A,N'_B} P_{N_A} P_{N_B} \frac{(1)(N_A)(N'_A)(N_B)(N'_B)}{(L_A)(L_B)(L)} \\ \times \begin{pmatrix} N_A & L_A & N'_A \\ \Lambda_A & K_A & -\Lambda'_A \end{pmatrix}^2 \begin{pmatrix} N_B & L_B & N'_B \\ \Lambda_B & K_B & -\Lambda'_B \end{pmatrix}^2 VG_{L_A,L_B,\lambda,L}(\Delta\omega - \omega_{\rm rot}), \end{aligned} \quad (32)$$

where $\hbar\omega_{\rm rot} = E'_{\rm rot} - E_{\rm rot}$. At negative detuning, we have

$$
\begin{aligned}
Vg(\omega_0 - \Delta\omega) \approx & \sum_{L_A,L_B,\lambda,L} \sum_{N_A,N_B,N'_A,N'_B} \exp\left(-\frac{\hbar\omega_{\rm rot}}{kT}\right) P_{N'_A} P_{N'_B} \frac{(1)(N_A)(N'_A)(N_B)(N'_B)}{(L_A)(L_B)(L)} \\
& \times \begin{pmatrix} N_A & L_A & N'_A \\ \Lambda_A & K_A & -\Lambda'_A \end{pmatrix}^2 \begin{pmatrix} N_B & L_B & N'_B \\ \Lambda_B & K_B & -\Lambda'_B \end{pmatrix}^2 VG_{L_A,L_B,\lambda,L}(-\Delta\omega - \omega_{\rm rot}). \\
& \approx \sum_{L_A,L_B,\lambda,L} \sum_{N_A,N_B,N'_A,N'_B} P_{N_A} P_{N_B} \frac{(1)(N_A)(N'_A)(N_B)(N'_B)}{(L_A)(L_B)(L)} \\
& \times \begin{pmatrix} N_A & L_A & N'_A \\ \Lambda_A & K_A & -\Lambda'_A \end{pmatrix}^2 \begin{pmatrix} N_B & L_B & N'_B \\ \Lambda_B & K_B & -\Lambda'_B \end{pmatrix}^2 \exp\left(+\frac{\hbar\omega_{\rm rot}}{kT}\right) VG_{L_A,L_B,\lambda,L}\left(-\left[\Delta\omega - \omega_{\rm rot}\right]\right) \\
& \approx \sum_{L_A,L_B,\lambda,L} \sum_{N_A,N_B,N'_A,N'_B} P_{N_A} P_{N_B} \frac{(1)(N_A)(N'_A)(N_B)(N'_B)}{(L_A)(L_B)(L)} \\
& \times \begin{pmatrix} N_A & L_A & N'_A \\ \Lambda_A & K_A & -\Lambda'_A \end{pmatrix}^2 \begin{pmatrix} N_B & L_B & N'_B \\ \Lambda_B & K_B & -\Lambda'_B \end{pmatrix}^2 \exp\left(-\frac{\hbar\Delta\omega}{kT}\right) VG_{L_A,L_B,\lambda,L}(\Delta\omega - \omega_{\rm rot}) \\
& \approx \exp\left(-\frac{\hbar\Delta\omega}{kT}\right) Vg(\omega_0 + \Delta\omega). \qquad (33)
\end{aligned}
$$

In the first step, we evaluate Eq. (6) at negative detuning and assume

$$P_{N_A} P_{N_B} \approx P_{N'_A} P_{N'_B} \exp\left(-\frac{\hbar\omega_{\rm rot}}{kT}\right), \qquad (34)$$

which is approximate as the primed and unprimed quantum numbers implicitly refer to different vibronic states. In the second step, we interchange primed and unprimed rotational quantum numbers, which are summed over. This neglects a possible change in Λ quantum number, which also affects the range of rotational states summed over, as well as possible restrictions to even or odd values of the rotational quantum numbers. In the third step, we use the approximate detailed balance relation for the translational profile, Eq. (31), to obtain

$$Vg(\omega_0 - \Delta\omega) \approx \exp\left(-\frac{\hbar\Delta\omega}{kT}\right) Vg(\omega_0 + \Delta\omega), \qquad (35)$$

an approximate detailed balance relation for the spectral density.

As noted above, we assume that the detuning is small, $|\Delta\omega| \ll \omega_0$, such that we have

$$\frac{\alpha(\omega_0 + \Delta\omega)}{\alpha(\omega_0 - \Delta\omega)} \approx \frac{Vg(\omega_0 + \Delta\omega)}{Vg(\omega_0 - \Delta\omega)} \approx \exp\left(\frac{\hbar\Delta\omega}{kT}\right), \qquad (36)$$

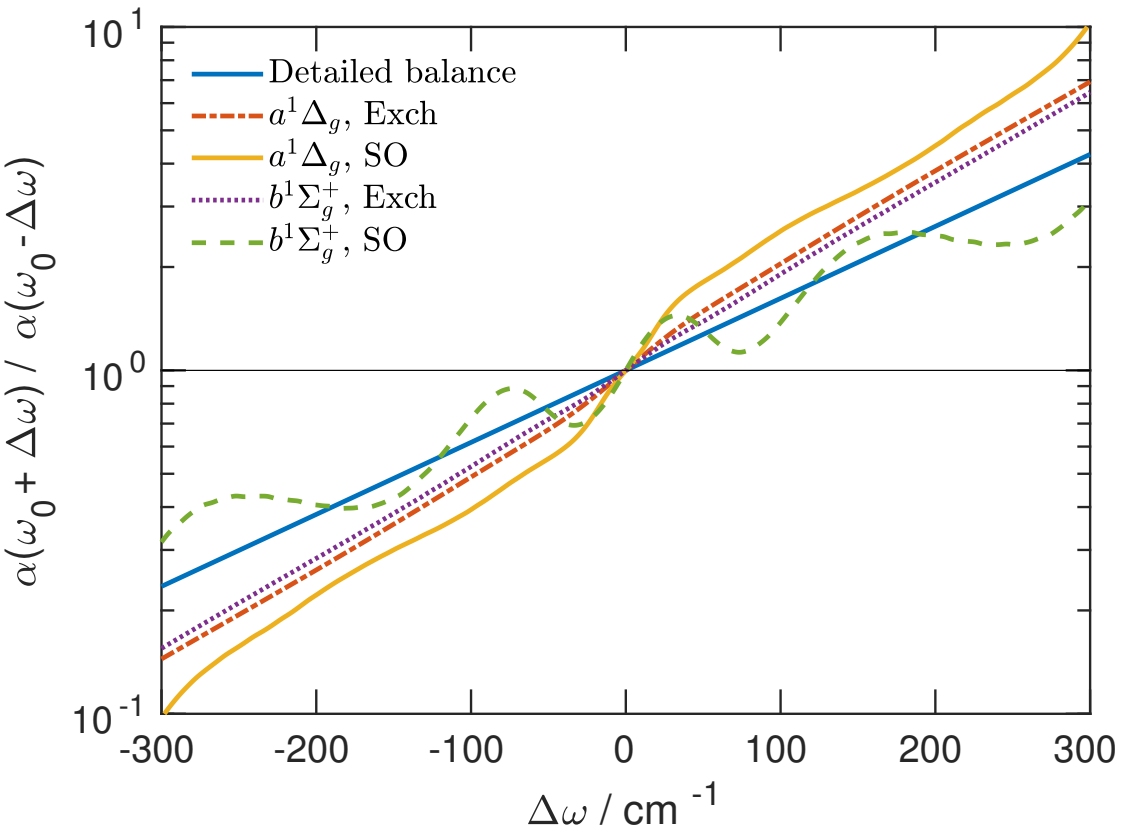

Figure 1. The fraction $\frac{\alpha(\omega_0+\Delta\omega)}{\alpha(\omega_0-\Delta\omega)}$ as a function of detuning, $\Delta\omega$, for both $X^3\Sigma_g^- \rightarrow a^1\Delta_g$ and $b^1\Sigma_g^+$ transitions, and for both mechanisms, which are compared to the prediction of the approximate detailed balance relations, Eq. (36).

that is, an approximate detailed balance relation for the absorption coefficient. This predicts that the "blue wing", at high frequency, of every vibronic band is stronger than the "red wing", at low frequency, by a Boltzmann factor, leading to a characteristic asymmetry. In Fig. 1, we compare the detailed balance prediction to the result of full line-shape calculations for both $X^3\Sigma_g^- \rightarrow a^1\Delta_g$ and $b^1\Sigma_g^+$ transitions, for both the exchange and spin-orbit mechanism. It is seen that the results of the full line shape calculations generally follow the approximate detailed balance relation, although some deviations are observed. Again, the approximate detailed balance relation, presented here, has been derived assuming that the initial and final state potential are identical. This is an accurate approximation for the isotropic potentials of $O_2 - O_2$, for the electronic states studied here.[1]

II. VIBRATIONAL DEPENDENCE OF DIPOLE SURFACE

To investigate the vibrational dependence of the $O_2 - O_2$ exchange-induced transition dipole moment, we have performed exploratory electronic structure calculations. In particular, we have performed calculations for fixed center-of-mass separation $R = 7\ a_0$, just outside the classical turning point of the isotropic potential, where we completely sample the angular coordinates described in Ref.[1], and include the vibrational coordinate of one molecule. This molecule is labeled A, and the bond length of the second molecule, B, is kept fixed at $r_B = 2.28\ a_0$. Next, we compute matrix elements for molecule A undergoing a $v'' = 0 \rightarrow v' = 1$ vibrational transition.

The results of these calculations are displayed in Table II, which shows "suppression factors" defined by

$$F_{L_A,L_B,\lambda,L}(v'_A, v'_B) = \left| \frac{\langle 00|\mathcal{D}_{L_A,L_B,\lambda,L}|v'_A v'_B\rangle}{\langle 00|\mathcal{D}_{L_A,L_B,\lambda,L}|00\rangle} \right|^2,$$
$$\langle v''_A v''_B|\mathcal{D}|v'_A v'_B\rangle = \int\int \psi^*_{v''_A}(r_A)\psi^*_{v''_B}(r_B)\mathcal{D}(r_A, r_B, R)\psi_{v'_A}(r_A)\psi_{v'_B}(r_B)\ r_A^2 dr_A\ r_B^2 dr_B, \quad (37)$$

that is, the ratios of the $v'' = 0 \rightarrow v' = 1$ and $v'' = 0 \rightarrow v' = 0$ squared transition dipole moments. These are shown for different angular expansion terms, labeled by $\{L_A, L_B, \lambda, L\}$, which contribute significantly to the absorption. For $X^3\Sigma_g^- \rightarrow a^1\Delta_g$, these are $\{4, 0, 4, 3\}$ and $\{4, 0, 4, 5\}$, which contribute 26 % and 28 % (8 % and 33 %) [19 % and 38 %] to the $v'' = 0 \rightarrow v' = 0$ intensity at the MRCI (CIS) [RAS] level of theory. For $X^3\Sigma_g^- \rightarrow b^1\Sigma_g^+$, two important angular terms are $\{1, 0, 1, 1\}$ and $\{3, 0, 3, 3\}$, which contribute 28 % and 26 % (27 % and 31 %) [17 % and 21 %] to the $v'' = 0 \rightarrow v' = 0$ intensity at the same levels of theory. Especially for the $X^3\Sigma_g^- \rightarrow a^1\Delta_g$ band, the factor at both levels of theory is much larger than the corresponding Franck-Condon factor, and exceptionally high for $\{4, 0, 4, 5\}$ at the CIS level, where the contribution to the absorption is smaller. For the $X^3\Sigma_g^- \rightarrow b^1\Sigma_g^+$ band, the suppression factor is closer to the Franck-Condon value.

This gives an indication of the sensitivity to the vibrational coordinate, which explains the breakdown of the scaling with Franck-Condon factors for the exchange mechanism. These effects are not fully predictive of the relative intensities of different vibrational bands: Full vibrationally-dependent dipole surfaces are unavailable, which would be necessary to compute the absorption line-shapes and intensities. The suppression factors may also be sensitive to vibrational averaging of the second molecule, which is not included here. The

Table II. Suppression factors of Eq. (37), the ratios of the $v'' = 0 \rightarrow v' = 1$ and $v'' = 0 \rightarrow v' = 0$ squared dipole moments, calculated for various transitions and significant angular terms, $\{L_A, L_B, \lambda, L\}$, at the CIS and RAS level, and using Franck-Condon Factors (FCF).

Transition to	L_A	L_B	λ	L	CIS	RAS	FCF[16]
$a^1\Delta_g(v'=1) + X^3\Sigma_g^-(v'=0)$	4	0	4	3	0.415	0.182	0.013
	4	0	4	5	0.165	0.164	0.013
$X^3\Sigma_g^-(v'=1) + a^1\Delta_g(v'=0)$	0	4	4	3	0.240	0.126	0
	0	4	4	5	0.141	0.151	0
$b^1\Sigma_g^+(v'=1) + X^3\Sigma_g^-(v'=0)$	1	0	1	1	0.067	0.076	0.067
	3	0	3	3	0.059	0.073	0.067
$X^3\Sigma_g^-(v'=1) + b^1\Sigma_g^+(v'=0)$	0	1	1	1	0.000	0.019	0
	0	3	3	3	0.001	0.020	0

effects of anisotropy, which are discussed in the next section, are significant and may also affect various vibrational transitions differently.

To compare the above results to the experimentally observed suppression of $v' > 0$, we consider the following. All contributions in Table II, *i.e.*, all angular components and all vibronic bands $a^1\Delta_g/b^1\Sigma_g^+(v'=1) + X^3\Sigma_g^-(v'=0)$ and $X^3\Sigma_g^-(v'=1) + a^1\Delta_g/b^1\Sigma_g^+(v'=0)$, contribute incoherently to the absorption, see Eq. (6). However, different angular components contribute with different prefactors that also depend on thermal populations of rotational levels, and we will therefore consider each angular term separately. First considering the $\{4,0,4,3\} + \{0,4,4,3\}$ contribution to the $X^3\Sigma_g^- \rightarrow a^1\Delta_g$ transition, adding both vibronic bands, we obtain suppression factors of 0.65 and 0.31 at the CIS and RAS level, respectively. For $\{4,0,4,5\} + \{0,4,4,5\}$ we obtain 0.21 and 0.31 at the CIS and RAS level, respectively. In view of the approximations discussed above, this is in agreement with the *total* experimental suppression factor of $X^3\Sigma_g^- \rightarrow a^1\Delta_g(v'=1)$ of 0.6, as seen in Table I of the main text. The suppression of individual terms does not need to be equal, and therefore may differ from the suppression of the *total* intensity, but it is reassuring that the suppression is of same order of magnitude for the angular terms, considered here, as these contribute significantly to the absorption. For the $\{1,0,1,1\} + \{0,1,1,1\}$ contribu-

tion to the $X^3\Sigma_g^- \rightarrow b^1\Sigma_g^+$ transition, the suppression factors are 0.07 and 0.10, and for $\{3,0,3,3\}+\{0,3,3,3\}$ the suppression factors are 0.06 and 0.09, at the CIS and RAS levels, respectively. This is again in qualitative agreement with the *total* suppression factor for $X^3\Sigma_g^- \rightarrow b^1\Sigma_g^+(v'=1)$ of 0.11, seen in Table I of the main text.

III. INTERACTION ANISOTROPY

In this section, we discuss a method for calculating integrated intensities of collision-induced absorption spectra, which is similar to that in Ref.[19] and references therein. This classical statistical mechanical theory is computationally not demanding, and can be applied efficiently using either isotropic or anisotropic potentials, unlike the quantum-mechanical line-shape calculations. Here, this approach is extended to vibronic transitions and applied to estimate the effect of interaction anisotropy on overall intensities. The ratio of intensities between anisotropic and isotropic calculations, calculated classically, is then used to scale absorption spectra from isotropic quantum line shape calculations. This correction for anisotropy is shown to perform well for roto-translational transitions of N_2-N_2, where both isotropic and anisotropic calculations have been performed.[5] We note that spectral moments can also be computed including quantum mechanical corrections,[20] but this is not attempted here.

A. Formalism

The collision-induced absorption coefficient is given by Eq. (1), in terms of the spectral density of Eq. (2). This spectral density represents a thermal average of the squared transition dipole moment between initial and final states, $|i\rangle$ and $|f\rangle$, with energies $\hbar\omega_i$ and $\hbar\omega_f$. These initial and final states will be thought of as products of functions of rotational and translational degrees of freedom (r.t.) – which we will treat classically below – and vibronic states (v.e.) – treated quantum mechanically throughout. That is, we have

$$\begin{aligned} |i\rangle &= |i_{\text{r.t.}}\rangle|i_{\text{v.e.}}\rangle, \\ |f\rangle &= |f_{\text{r.t.}}\rangle|f_{\text{v.e.}}\rangle. \end{aligned} \tag{38}$$

For simplicity we consider the case where a single initial and a single final vibronic state contribute to any particular collision-induced band. Where multiple vibronic transitions

contribute, their contributions can be added incoherently. Introducing the transition dipole moment surface, $\hat{\boldsymbol{\mathcal{D}}} = \langle f_{\mathrm{v.e.}}|\hat{\boldsymbol{\mu}}|i_{\mathrm{v.e.}}\rangle$, we may write

$$Vg(\omega,T) = V \sum\!\!\!\!\!\!\int_{i_{\mathrm{r.t.}}} \sum\!\!\!\!\!\!\int_{f_{\mathrm{r.t.}}} P^{(i_{\mathrm{r.t.}})}(T)|\langle f_{\mathrm{r.t.}}|\hat{\boldsymbol{\mathcal{D}}}|i_{\mathrm{r.t.}}\rangle|^2 \delta(\omega_{f_{\mathrm{r.t.}}} - \omega_{i_{\mathrm{r.t.}}} - \omega), \tag{39}$$

where the sums and integrals now extend only over the rotational and translational degrees of freedom as indicated.

Dropping the "r.t." subscript, the integral of the spectral density over all frequencies is given by

$$\begin{aligned}\int_{-\infty}^{\infty} d\omega V g(\omega,T) &= V \sum\!\!\!\!\!\!\int_i \sum\!\!\!\!\!\!\int_f P^{(i)}(T)|\langle f|\hat{\boldsymbol{\mathcal{D}}}|i\rangle|^2 \int_{-\infty}^{\infty} d\omega \delta(\omega_f - \omega_i - \omega) \\ &= V \sum\!\!\!\!\!\!\int_i \sum\!\!\!\!\!\!\int_f P^{(i)}(T)\langle i|\hat{\boldsymbol{\mathcal{D}}}^\dagger|f\rangle \cdot \langle f|\hat{\boldsymbol{\mathcal{D}}}|i\rangle. \end{aligned} \tag{40}$$

Now if we assume a completeness relation for the final-state radial wavefunctions

$$\sum\!\!\!\!\!\!\int_f |f\rangle\langle f| = 1, \tag{41}$$

the above integral simplifies to

$$\begin{aligned}\int_{-\infty}^{\infty} d\omega V g(\omega,T) &= V \sum\!\!\!\!\!\!\int_i P^{(i)}(T)\langle i|\hat{\boldsymbol{\mathcal{D}}}^\dagger \cdot \hat{\boldsymbol{\mathcal{D}}}|i\rangle, \\ &= \frac{V}{Q(T)} \mathrm{Tr}\left[\exp\left(-\hat{H}/k_B T\right) \hat{\boldsymbol{\mathcal{D}}}^\dagger \cdot \hat{\boldsymbol{\mathcal{D}}}\right] \end{aligned} \tag{42}$$

in which one recognizes the thermal average of the squared transition dipole moment, $\hat{\boldsymbol{\mathcal{D}}}^\dagger \cdot \hat{\boldsymbol{\mathcal{D}}}$. Where Tr denotes the trace over all rotation-translation coordinates.

It is useful to introduce $\hat{H} = \hat{H}_0 + \hat{\mathcal{V}}$, that is, to write the total Hamiltonian, $\hat{H}$, as the sum of monomer Hamiltonians, $\hat{H}_0$, and the interaction potential, $\hat{\mathcal{V}}$, and to write the partition sum as

$$Q(T) = \mathrm{Tr}\left[\exp\left(-\hat{H}_0/k_B T\right)\right]. \tag{43}$$

For the rotation-translation coordinates considered here, the monomer Hamiltonians $\hat{H}_0$ contain kinetic energy terms only.

The thermal average can be approximated using the classical limit, where the trace is replaced by a phase space integral. In this classical approximation, $\exp(-H/k_B T) =$

$\exp(-H_0/k_BT)\exp(-\mathcal{V}/k_BT)$, and the integrals over the conjugate momenta in the trace in Eq. (42) cancel against those in the partition sum. Hence, we are left with integrals over the nuclear coordinates only

$$\int_{-\infty}^{\infty} d\omega V g(\omega,T) \approx V \frac{\int\int\int \exp(-\mathcal{V}/k_BT)\boldsymbol{\mathcal{D}}^\dagger\cdot\boldsymbol{\mathcal{D}}\; d\boldsymbol{R}d\Omega_A d\Omega_B}{\int\int\int\; d\boldsymbol{R}d\Omega_A d\Omega_B}$$
$$= \frac{\int\int\int \exp(-\mathcal{V}/k_BT)\boldsymbol{\mathcal{D}}^\dagger\cdot\boldsymbol{\mathcal{D}}\; d\boldsymbol{R}d\Omega_A d\Omega_B}{\int\int\; d\Omega_A d\Omega_B} \tag{44}$$

To be completely explicit, for the case of two diatomic molecules, A and B, one has

$$\int_{-\infty}^{\infty} d\omega V g(\omega,T) = \frac{1}{8\pi}\int_0^\infty 4\pi R^2 dR \int_{-1}^{1} d\cos(\theta_A)\int_{-1}^{1} d\cos(\theta_B)\int_0^{2\pi} d\phi \exp(-\mathcal{V}/k_BT)\hat{\boldsymbol{\mathcal{D}}}^\dagger\cdot\hat{\boldsymbol{\mathcal{D}}}, \tag{45}$$

where R is the distance between the centers of mass of molecules A and B, θ_X is the angle between the intermolecular axis and the bond-axis of molecule $X = A, B$, and ϕ is the dihedral angle.

B. Numerical results

Table III shows numerical results for the $O_2 - O_2$ collision-induced intensities, obtained by either integrating the absorption spectrum from quantum line-shape calculations, or directly from the classical statistical mechanical theory described above. The result from the isotropic calculations agree well, with the deviations between line-shape and classical statistical mechanical calculations being largest for lowest temperatures. The intensities calculated for anisotropic interaction potentials are systematically larger. The increase in intensity is substantial, by a factor of 2 to 4 at room temperature, and by larger factors at lower temperatures.

We note that we have also applied this approach to the roto-translational band of N_2-N_2. In this case, we find a 20 % enhancement of the intensity at $T = 78\ K$, and essentially no effect at room temperature, in agreement with the full line-shape calculations of Ref.[5]. Clearly, the effects of anisotropic interactions are more substantial for the electronic transitions considered here. The differences with the roto-translational band, of $N_2 - N_2$ for example, lie both in the radial and angular dependence of the dipole surface.

On the anisotropic potential, the molecules approach more closely for attractive orientations. Because the transition dipole moment for electronic transitions considered here

Table III. Intensities for O_2-O_2 obtained by integrating the line profile from line-shape calculations, and those obtained from the statistical mechanical theory. Results for the statistical theory are given for both the isotropic part of the potential, and for the full anisotropic potential energy surface. Integrated intensities are given in $cm^{-2}amagat^{-2}$ with numbers in parentheses denoting powers of ten.

	$T = 300$ K	$T = 200$ K	$T = 100$ K
$X^3\Sigma_g^- \rightarrow a^1\Delta_g$			
MRCI dipole surface			
Line-shape calculation	2.75 (−5)	2.06 (−5)	1.41 (−5)
Intensity calculation, isotropic potential	2.93 (−5)	2.23 (−5)	1.87 (−5)
Intensity calculation, anisotropic potential	6.85 (−5)	5.42 (−5)	5.21 (−5)
CASSCF dipole surface			
Line-shape calculation	2.15 (−5)	1.59 (−5)	1.09 (−5)
Intensity calculation, isotropic potential	2.28 (−5)	1.73 (−5)	1.44 (−5)
Intensity calculation, anisotropic potential	6.06 (−5)	4.82 (−5)	4.65 (−5)
$X^3\Sigma_g^- \rightarrow b^1\Sigma_g^+$			
MRCI dipole surface			
Line-shape calculation	1.80 (−6)	1.15 (−6)	6.55 (−7)
Intensity calculation, isotropic potential	1.89 (−6)	1.20 (−6)	7.79 (−7)
Intensity calculation, anisotropic potential	6.67 (−6)	2.72 (−6)	2.22 (−6)
CASSCF dipole surface			
Line-shape calculation	5.76 (−7)	3.83 (−7)	2.28 (−7)
Intensity calculation, isotropic potential	5.98 (−7)	3.99 (−7)	2.75 (−7)
Intensity calculation, anisotropic potential	2.13 (−6)	1.64 (−6)	1.55 (−6)

is exponentially R-dependent, this leads to a substantial increase in dipole moment. For roto-translational bands, where the R-dependence is dominantly R^{-4}, this effect is less substantial.

The angular dependence of the contribution to the absorption is subject to symmetry restrictions. For roto-translational bands, parallel orientations do not contribute to the absorption, and the contribution to the intensity is dominated by T-shaped orientations.

The anisotropic potential for T-shaped orientations is typically very close to the isotropic potential, albeit slightly more attractive, such that only a small increase due to anisotropic interactions is expected. For electronic transitions, on the other hand, the symmetry restrictions are different, such that there are contributions from parallel orientations. For these parallel orientations, the anisotropic potential is qualitatively different from the isotropic potential, as the classical turning point occurs at much shorter separation, for example. Therefore, larger effects of anisotropic interactions are observed.

To further investigate the effect of anisotropy, we have performed line-shape calculations using a radially-shifted isotropic potential. In order to obtain agreement of the total intensity, a shift of 0.6-0.7 a_0 is required. This shift is small compared to the neglected anisotropy of the classical turning point of the potential, which varies between 7.5 a_0 for collinear geometries, and 5.4 a_0 for parallel orientations.

IV. ADDITIONAL EXCHANGE-INDUCED TRANSITION DIPOLE MOMENT SURFACES

In order to estimate the effect of uncertainty in the transition dipole moment on the calculated absorption spectra, we have calculated three additional intermolecular-exchange-induced dipole surfaces for $O_2 - O_2$. The computational approaches are as follows:

- *l*CAS: Complete active space self-consistent field calculation including all $2s$ and $2p$ valence orbitals except the $2p\sigma^*$ orbitals.

- RAS: Restricted active space self-consistent field (RASSCF) calculation with 4 electrons in the $2p\sigma$ and $2p\sigma^*$ orbitals, and 12 electrons in the $2p\pi$ and $2p\pi^*$ orbitals. This includes $\sigma \rightarrow \sigma^*$ and $\pi \rightarrow \pi^*$ correlation, involved in breaking inversion symmetry, which may be thought important in describing the parity forbidden transition dipole moments.

- CIS: Uses the minimal π^* active space description for the states of interest, and single excitations from these reference wavefunctions.

These calculations were all performed in a split-valence 6-31G basis set, and carried out using the MOLPRO 2012 package.[21]

These dipole moment surfaces were calculated and fit similar to the MRCI and CASSCF dipole surfaces of Ref.[1]. We used the multiple-property-based diabatization algorithm of Ref.[22] to transform the *ab initio* transition dipoles from the adiabatic to a diabatic representation. The radial grid contains R = 5.5, 5.75, 6, 6.25, 6.5, 6.75, 7, 7.25, 7.5, 7.75, and 8 a_0. For each separation, 150 orientations were sampled using Gauss-Legendre and Gauss-Chebyshev quadrature points in the Jacobi angles. This allowed us to accurately calculate angular expansion coefficients using numerical integration, and subsequently fit their radial dependence using the exponential interpolation scheme detailed in Ref.[1].

We have performed scattering calculations of absorption spectra using these five transition dipole surfaces. The resulting collision-induced absorption spectra are shown in Fig. 4 of the main text. These result in predictions for the overall intensity which vary by factors 7 to 10. Clearly, the intensity cannot be predicted from first principles without improving electronic structure methods for calculating the intermolecular-exchange-induced dipole moment. The scaling factors required to obtain agreement between experiment and theory, reported in Table I of the main text, are smaller than this estimate of the uncertainty of the calculation. Therefore, the experiment and theory can be said to agree to within the "theoretical error bars". Furthermore, the scaling factors obtained for the spin-orbit based mechanism are generally much closer to unity, which is consistent with the reduced uncertainty of the transition dipole moment for this mechanism: Within the assumed long-range model, the spin-orbit-induced transition dipole moment is given completely in terms of accurately known monomer properties.

The scattering calculations presented here, employing different dipole surfaces, consistently predict the same line shape. This implies that the predicted line shape is unaffected by the uncertainty in the calculations. This can be understood as the width qualitatively reflects the interaction time-scale, and hence the length scale of the dipole surface. The typical length scale of exponential decay of the transition dipole moment is predicted consistently, resulting in nearly identical absorption line shapes, although the transition dipole surface are not converged.

V. FITTING OF EXPERIMENTAL SPECTRA

This section describes how the theoretical line shapes were fit to the experimental results, *i.e.*, how the scale factors of Table I of the main text were obtained. First, the theoretical absorption spectra computed in the isotropic interaction approximation were corrected for anisotropic interactions. This was accomplished by scaling with the ratio of integrated intensity computed including and excluding anisotropy. These integrated intensities are computed as described in Sec. III, and displayed in Table III. Subsequently, we performed an unconstrained linear least squares fit to the experimental data points, with equal weights. The scaling factors for the exchange and/or spin-orbit contributions were treated as the linear fit parameters.

For the $v' = 0 \rightarrow v'' = 0$ bands of $O_2 - O_2$, we included both mechanisms. For $O_2 - N_2$ we included only the spin-orbit line shape, which is the only contributing mechanism for this system. For $v'' > 0$ bands, the $O_2 - N_2$ contribution was not observed experimentally. For the $v' = 0 \rightarrow v'' > 0$ bands of $O_2 - O_2$ we included only the exchange line shape. The spin-orbit mechanism should contribute only weakly, on the same scale as for $O_2 - N_2$, and hence was excluded from the fit.

The resulting scale factors are shown Table I of the main text. We again point out that the scale factors – which include corrections for anisotropic interactions – are of order unity for the spin-orbit mechanism, whereas the exchange contributions required scalings which are within the uncertainty due to inaccuracies of the exchange-induced dipoles, estimated in the previous section.

VI. EXPERIMENT

Here, we describe measurements of the $a^1\Delta_g(v' = 1)$ band in $O_2 - O_2$ and $O_2 - N_2$, shown in Fig. 1 panel (b) of the main text, using cavity ring-down spectroscopy similar to that in Ref.[23].

A Toptica DL100 grating stabilized diode laser with a LD-1060-0150-AR-2 diode was used as a light source. The output power was 170 mW in the spectral range of $9\,259 - 9\,569$ cm^{-1}. About 2 % of the beam was split off by a glass plate and guided into a wavelength meter. The cavity was placed inside a pressure cell which was designed to hold pressures from 10^{-3}

to 8 bar. The pressure inside the cavity was measured using a diaphragm pressure detector (Pfeiffer Vacuum D-35614). The gas flow towards the pressure cell was controlled by a Digital Thermal Mass Flow Controller (El-Flow, Bronkhorst high tech). The outlet for the gas was connected to a membrane vacuum pump (Pfeifer Vacuum MVP 055-3) with which it was possible to reach pressures as low as 1 mbar. The cavity mirrors (Layertec) had a reflectivity above 99.993% in the range of $9\,100 - 9\,900$ cm^{-1} and a radius of curvature of 8 000 mm. The cavity length was 35.0 cm, creating an effective path length of about 5 km. The light leaving the cavity was captured using an avalanche photo-diode. The signals from this detector were sent to a SRS signal generator to trigger the ring-down events.

For each collision-induced absorption measurement, the lasing frequency was set at a specific value. To reduce the uncertainty, wavelengths without water absorptions were selected. The sample gas was guided into the pressure cell at a fixed rate of 200 mL/min resulting in pressure ramps from 0 to 8 bar. During the pressure ramps the cavity ring-down signals were recorded continuously and were kept at a constant rate of about 3 signals per second. This resulted in 1500-2000 decay signals for each pressure ramp. The decay signals were then fitted with an exponential function to give the decay times. The collision-induced absorption was then obtained by fitting a second-order polynomial function to the pressure dependence of the decay time, ensuring that the fitted decay corresponds to two-body absorption. In total 34 pressure ramps were performed for pure O_2 (6.0 Purity) and 52 in air (22.316 ± 0.022 % O_2). Lastly, since the collision-induced absorption of oxygen transitions is much smaller in air, a lens with a focus of 25 cm had to be placed in front of the cavity to ensure only the lowest cavity modes were accessed. This enhanced the accuracy of the set-up significantly.

REFERENCES

[1]Karman, T., van der Avoird, A. & Groenenboom, G. C. Potential energy and dipole moment surfaces of the triplet states of the $O_2(X^3\Sigma_g^-) - O_2(X^3\Sigma_g^-, a^1\Delta_g, b^1\Sigma_g^+)$ complex. *J. Chem. Phys.* **147**, 084306 (2017).

[2]Karman, T., van der Avoird, A. & Groenenboom, G. C. Line-shape theory of the $X^3\Sigma_g^- \rightarrow a^1\Delta_g, b^1\Sigma_g^+$ transitions in O_2-O_2 collision-induced absorption. *J. Chem. Phys.* **147**, 084307 (2017).

[3]Gustafsson, M., Frommhold, L., Bailly, D., Bouanich, J.-P. & Brodbeck, C. Collision-induced absorption in the rototranslational band of dense hydrogen gas. *J. Chem. Phys.* **119**, 12264 (2003).

[4]Karman, T., van der Avoird, A. & Groenenboom, G. C. Collision-induced absorption with exchange effects and anisotropic interactions: theory and application to H_2-H_2. *J. Chem. Phys.* **142**, 084305 (2015).

[5]Karman, T., Miliordos, E., Hunt, K. L. C., Groenenboom, G. C. & van der Avoird, A. Quantum mechanical calculation of the collision-induced absorption spectra of N_2-N_2 with anisotropic interactions. *J. Chem. Phys.* **142**, 084306 (2015).

[6]Hartmann, J.-M., Boulet, C. & Jacquemart, D. Molecular dynamics simulations for CO_2 spectra. II. the far infrared collision-induced absorption band. *J. Chem. Phys.* **134**, 094316 (2011).

[7]Bussery-Honvault, B. & Hartmann, J.-M. Ab initio calculations for the far infrared collision induced absorption by N_2 gas. *J. Chem. Phys.* **140**, 054309 (2014).

[8]Frommhold, L. *Collision-Induced Absorption in Gases* (Cambridge Univ. Press, Cambridge, 1994).

[9]Bartolomei, M., Carmona-Novillo, E., Hernández, M. I., Campos-Martínez, J. & Moszyński, R. Global ab initio potential energy surface for the $O_2(^3\Sigma_g^-)$ + $N_2(^1\Sigma_g^+)$ interaction. applications to the collisional, spectroscopic, and thermodynamic properties of the complex. *J. Phys. Chem. A* **118**, 6584 (2014).

[10]Bartolomei, M., Carmona-Novillo, E., Hernández, M. I., Campos-Martínez, J. & Hernández-Lamoneda, R. Global *ab initio* potential energy surfaces for the $O_2(^3\Sigma_g^-)$+$O_2(^3\Sigma_g^-)$ interaction. *J. Chem. Phys.* **133**, 124311 (2010).

[11]Minaev, B. Intensities of spin-forbidden transitions in molecular oxygen and selective heavy- atom effects. *Int. J. Quantum Chem.* **XVII**, 367 (1980).

[12]Minaev, B., Vahtras, O. & Ågren, H. Magnetic phosphorescence of molecular oxygen. A study of the $b^1\Sigma_g^+$-$X^3\Sigma_g^-$ transition probability using multiconfiguration response theory. *Chem. Phys.* **208**, 299–311 (1996). URL `http://www.sciencedirect.com/science/article/pii/0301010496001267`.

[13]Grimminck, D. L. A. G. *et al.* A theoretical and experimental study of pressure broadening of the oxygen A-band by helium. *J. Chem. Phys.* **140**, 204314 (2014).

[14]Gordon, I. E., Kassi, S., Campargue, A. & Toon, G. C. First identification of the electric

quadrupole transitions of oxygen in solar and laboratory spectra. *J. Quant. Spectrosc. Radiat. Transfer* **111**, 1174 (2010).

[15]Tipping, R., Ma, Q., Boulet, C. & Hartmann, J.-M. Theoretical analysis of the collision-induced electronic absorptions in O_2-N_2 and O_2-CO_2 pairs. *J. Mol. Struct.* **742**, 83 (2005).

[16]Nichols, R. Franck-condon factors to high vibrational quantum numbers V: O2 band systems. *J. Res. Nat. Bur. Stand. Sec. A Phys. Ch.* **69A**, 369 (1965).

[17]Olver, F. W. J., , Lozier, D. W., Boisvert, R. F. & Clark, C. W. *The NIST Handbook of Mathematical Functions* (Cambridge Univ. Press, 2010).

[18]Johnson, B. R. The log-derivative and renormalized numerov algorithms. *NRCC Proceedings* **5**, 86 (1979).

[19]Buryak, I., Lokshtanov, S. & Vigasin, A. CCSD(T) potential energy and induced dipole surfaces for N_2-$H_2(D_2)$: Retrieval of the collision-induced absorption integrated intensities in the regions of the fundamental and first overtone vibrational transitions. *J. Chem. Phys.* **137**, 114308 (2012).

[20]Moraldi, M. & Frommhold, L. Collision-induced infrared absorption by H_2-He complexes: Accounting for the anisotropy of the interaction. *Phys. Rev. A* **52**, 274 (1995).

[21]Werner, H.-J. & P. J. Knowles *et al.* MOLPRO: a package of ab initio programs, version 2012.1. URL `http://www.molpro.net`.

[22]Karman, T., van der Avoird, A. & Groenenboom, G. C. Communication: Multiple-property-based diabatization for open-shell van der waals molecules. *J. Chem. Phys.* **144**, 121101 (2016).

[23]Spiering, F. R. *et al.* Line mixing and collision induced absorption in the oxygen A-band using cavity ring-down spectroscopy. *J. Chem. Phys.* **133**, 114305 (2010).